Inorganic Chemistry

Article

pubs.acs.org/IC

Homoleptic Nickel(II) Complexes of Redox-Tunable Pincer-type Ligands

Jeewantha S. Hewage,[†] Sarath Wanniarachchi,[†] Tyler J. Morin,[†] Brendan J. Liddle,[†] Megan Banaszynski,[†] Sergey V. Lindeman,[†] Brian Bennett,*[,‡] and James R. Gardinier*[,†]

[†]Department of Chemistry, Marquette University, Milwaukee, Wisconsin 53201-1881, United States

[‡]Department of Biophysics, Medical College of Wisconsin, Milwaukee, Wisconsin 53226, United States

Supporting Information

ABSTRACT: Different synthetic methods have been developed to prepare eight new redox-active pincer-type ligands, H(X,Y), that have pyrazol-1-yl flanking donors attached to an *ortho*-position of each ring of a diarylamine anchor and that have different groups, X and Y, at the *para*-aryl positions. Together with four previously known H(X,Y) ligands, a series of 12 $Ni(X,Y)_2$ complexes were prepared in high yields by a simple one-pot reaction. Six of the 12 derivatives were characterized by single-crystal X-ray diffraction, which showed tetragonally distorted hexacoordinate nickel(II) centers. The nickel(II) complexes exhibit two quasi-reversible one-electron oxidation waves in their cyclic voltammograms, with half-wave potentials that varied over a remarkable 700 mV range with the average of the Hammett σ_p parameters of the *para*-aryl X, Y groups. The one- and two-electron oxidized derivatives $[Ni(Me,Me)_2](BF_4)_n$ (n = 1, 2) were prepared synthetically, were characterized by X-band EPR, electronic spectroscopy, and single-crystal X-ray diffraction (for n = 2), and were studied computationally by DFT methods. The dioxidized complex, $[Ni(Me,Me)_2](BF_4)_2$, is an S = 2 species, with nickel(II) bound to two ligand radicals. The mono-oxidized complex $[Ni(Me,Me)_2](BF_4)$, prepared by comproportionation, is best described as nickel(II) with one ligand centered radical. Neither the mono- nor the dioxidized derivative shows any substantial electronic coupling between the metal and their bound ligand radicals because of the orthogonal nature of their magnetic orbitals. On the other hand, weak electronic communication occurs between ligands in the mono-oxidized complex as evident from the intervalence charge transfer (IVCT) transition found in the near-IR absorption spectrum. Band shape analysis of the IVCT transition allowed comparisons of the strength of the electronic interaction with that in the related, previously known, Robin−Day class II mixed valence complex, $[Ga(Me,Me)_2]^{2+}$.

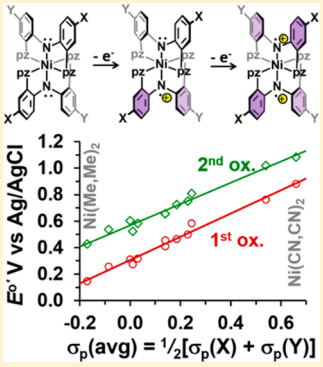

INTRODUCTION

There has been long-standing interest in metal complexes of redox-active "noninnocent" ligands[1] that persists because of the enticing prospects for advancing fundamental knowledge of electronic structure and bonding,[2] for discovering new reactivity that may arise from both metal and ligand-centered electron transfer,[3] or for the development of new technological applications that rely on electron (or hole) transfer.[4] Control over the syntheses and electrochemical properties of new classes of redox-active ligands and their metal complexes is important for making advances in either fundamental or applied areas of study. While a majority of such studies have focused on metal complexes of bidentate noninnocent ligands,[5] those involving terdentate "pincer" ligands are gaining prominence.[6−18] Among these, the chemical and redox noninnocence of metal complexes of the bis(imino)pyridine "pincer" ligand has been exploited to produce a number of remarkable chemical transformations.[7] Metal pincer complexes with redox-active diarylamido anchors are also gaining popularity for their spectacular reaction chemistry.[6,8−18] We have been studying the properties of metal complexes of a new class of redox-active pincer-type ligand that has pyrazolyl flanking donors attached to a diarylamido anchor, as in Figure 1.[19]

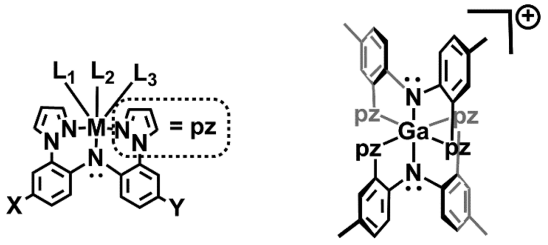

Figure 1. Metal complexes of pyrazolyl-containing redox-active pincer ligands.

These uninegative pincer-type ligands will be described herein by the shorthand notation $(X,Y)^-$ that denotes the substitution at the *para*-aryl positions (X and Y, left of Figure 1) of the diarylamido backbone. In rhodium chemistry, complexes $(Me,Me)Rh(L_1)(L_2)(L_3)$ showed ligand-centered oxidations that occurred at potentials that depended on the charge of the complex and the Lever parameter (E_L) of nonpincer ligands L_1, L_2, and L_3.[19b] Also, for a series of carbonylrhodium(I)

Received: March 21, 2014
Published: September 15, 2014

   dx.doi.org/10.1021/ic500657e | *Inorg. Chem.* 2014, 53, 10070−10084

Table 1. Crystallographic Data Collection and Structure Refinement for Ni(Me,Me)$_2$, 1, Ni(H,H)$_2$·CH$_2$Cl$_2$, 3·CH$_2$Cl$_2$, Ni(Me,Br)$_2$, 4, and Ni(Me,CF$_3$)$_2$, 6

	compound			
	1	3·CH$_2$Cl$_2$	4	6
formula	$C_{40}H_{36}N_{10}Ni$	$C_{37}H_{30}Cl_2N_{10}Ni$	$C_{38}H_{30}Br_2N_{10}Ni$	$C_{40}H_{34}F_6N_{10}Ni$
formula weight	715.50	744.32	845.25	823.458
crystal system	triclinic	monoclinic	triclinic	triclinic
space group	$P\bar{1}$	$P2_1/n$	$P\bar{1}$	$P\bar{1}$
temp [K]	100(2)	100(2)	100(2)	100(2)
a [Å]	8.7592(2)	9.55338(11)	8.7709(3)	8.9877(2)
b [Å]	12.8293(3)	17.50145(18)	12.8252(4)	13.0879(2)
c [Å]	16.0382(3)	40.5845(5)	16.1692(5)	16.3390(3)
α [deg]	79.7090(10)	90.00	80.012(2)	79.7450(10)
β [deg]	84.0790(10)	93.2065(12)	83.860(2)	84.0600(10)
γ [deg]	75.7380(10)	90.00	76.027(2)	74.1850(10)
V [Å^3]	1715.33(6)	6775.02(13)	1734.24(10)	1816.60(6)
Z	2	8	2	2
D_{calcd} [g cm^{-3}]	1.385	1.459	1.619	1.505
λ [Å] (Cu or Mo Kα)	1.54178	1.54178	1.54178	1.54178
μ [mm^{-1}]	1.179	2.635	3.866	1.442
abs correction	numerical	multiscan	numerical	numerical
F(000)	748	3072	852	844
θ range [deg]	2.81−67.98	3.34−70.67	2.78−67.55	2.75−67.91
reflns collected	14 299	53 167	14 217	6167
indep reflns	5860 (R_{Int} = 0.0160)	12 822 (R_{Int} = 0.0303)	5894 (R_{Int} = 0.0208)	6167 (R_{Int} = 0.000)
T_min/max	0.6603/0.9034	0.63724/1.0	0.3161/0.8995	0.6492/0.8021
data/restraints/parameters	5860/0/464	12 822/0/902	5894/4/478	6167/0/571
GOF on F^2	1.000	1.037	1.244	1.054
R1[a]/wR2[b] [$I > 2\sigma(I)$]	0.0308/0.0788	0.0373/0.0860	0.0454/0.0963	0.0431/0.1095
R1[a]/wR2[b] (all data)	0.0331/0.0804	0.0467/0.0895	0.0491/0.0977	0.0447/0.1107
largest diff peak/hole/e·Å^{-3}	0.236/−0.310	0.673/−0.634	0.310/−0.348	0.620/−0.360

[a] $R1 = \sum||F_o| - |F_c||/\sum|F_o|$. [b] $wR2 = [\sum w(|F_o| - |F_c|)^2/\sum w|F_o|^2]^{1/2}$.

complexes, (X,Y)Rh(CO), the reactivity toward a given alkyl halide increased predictably with the electron-donating ability of the X and Y groups as indicated by the groups' Hammett σ_p parameter.[19c] More recently, the homoleptic gallium(III) complex [Ga(Me,Me)$_2$]$^+$ was reported, which showed two reversible one-electron oxidations in its voltammogram.[19a] The entire valence series was structurally and spectroscopically characterized. On the basis of electrochemical and spectroscopic studies, the one-electron oxidized [Ga(Me,Me)$_2$]$^{2+}$ was found to be a Robin−Day class II species where weak electronic communication between oxidized and nonoxidized ligands was thought to occur via superexchange through the empty orbitals on gallium. It was conjectured that replacing the gallium(III) center with a transition metal would greatly strengthen the electronic communication because the 3d-orbitals should be energetically accessible and allow for dπ−pπ interactions with the magnetic orbitals on the ligand. In addition to changing metals, we were also interested in determining whether changing the electronic properties (without changing the steric profile) of the redox-active pincer ligands would provide a means to alter the strength of electronic communication. Although we previously observed that changing *para*-aryl substituents can affect electronic properties in rhodium complexes, it was unclear whether this translated to first-row metals, and, more importantly, how much could the electronic properties be tuned. Could this tuning be enough to switch from a ligand- to a metal-centered redox process, or vice versa? This contribution discloses our first efforts in this vein, where eight new pincer ligands of the type H(X,Y) were prepared to allow a systematic study of the electronic properties of 12 nickel(II) complexes, Ni(X,Y)$_2$, with diverse *para*-aryl substituents. The electrochemical, spectroscopic properties, and computational studies on the complete valence series [Ni(Me,Me)$_2$]$^{n+}$ are documented. Comparison of properties between mixed-valent complexes [M(Me,Me)$_2$]$^{n+}$ (n = 1 for M = Ni and n = 2 for M = Ga) was made to elucidate the role of the metal center in mediating electronic communication.

EXPERIMENTAL SECTION

For space considerations, most of the ligand and nickel complex syntheses are found in the Supporting Information. A representative set of complexes using the previously described ligand H(Me,Me)[19] is found below. The oxidations were performed under Ar by using commercial ferrocenium tetrafluoroborate, FcBF$_4$, in dry, distilled CH$_2$Cl$_2$.

Nickel Complex Syntheses. *Ni(Me,Me)$_2$, 1.* An emerald green solution of 1.06 g (3.22 mmol) of H(Me,Me) and 1.23 g (1.61 mmol) of NiCl$_2$·6H$_2$O in 15 mL of MeOH was heated at reflux 10 min. Next, 0.70 mL of a 1.47 M (1.61 mmol) solution of (NEt$_4$)(OH) in MeOH was injected into the hot reaction mixture by syringe. The solution became dark forest green immediately upon mixing, and within 1 min copious orange-brown solid precipitated. After the orange-brown suspension had been heated at reflux 30 min, the mixture was allowed to cool to room temperature. The insoluble portion was collected by filtration, was washed with two 5 mL portions of Et$_2$O, and was dried by heating at 80 °C under vacuum 6 h to leave 1.10 g (95% yield) of **1** as a brown-orange solid. Mp, 350 °C dec to black liq. Anal. Calcd for $C_{40}H_{36}N_{10}Ni$: C, 67.15; H, 5.07; N, 19.59. Found: C, 67.18; H, 5.17; N, 19.59. μ_{eff} (solid, 295 K) = 2.9 μ_B. UV−vis (CH$_2$Cl$_2$) λ_{max}, nm (ε, M^{-1} cm^{-1}): 368 (51 600), 415 (21 200), 467 sh (640), 543 (180), 791

dx.doi.org/10.1021/ic500657e | Inorg. Chem. 2014, 53, 10070−10084

Table 2. Crystallographic Data Collection and Structure Refinement for $Ni(Me,CN)_2 \cdot 1.29CH_2Cl_2$, $8 \cdot 1.29CH_2Cl_2$, $Ni(CN,CN)_2 \cdot 2$acetone, $10 \cdot 2$acetone, and $Ni(CN,CN)_2 \cdot$acetone, $10 \cdot$acetone

	compound		
	$8 \cdot 1.29CH_2Cl_2$	**10**·2acetone	**10**·acetone
formula	$C_{41.3}H_{32.6}Cl_{2.6}N_{12}Ni$	$C_{46}H_{36}N_{14}NiO_2$	$C_{43}H_{30}N_{14}NiO$
formula weight	847.49	875.60	817.52
crystal system	monoclinic	triclinic	monoclinic
space group	$P2_1/n$	$P\bar{1}$	$P2_1/n$
temp [K]	100(2)	100.0(1)	100.0(1)
a [Å]	17.3591(3)	9.8514(2)	14.21320(17)
b [Å]	27.8741(5)	13.9696(3)	15.60318(16)
c [Å]	17.7477(3)	16.7096(4)	17.3945(2)
α [deg]	90.00	100.8347(18)	90.00
β [deg]	102.7148(19)	98.0479(18)	103.6602(13)
γ [deg]	90.00	91.2391(18)	90.00
V [Å^3]	8376.9(3)	2233.64(8)	3748.49(8)
Z	8	2	4
D_{calcd} [g cm^{-3}]	1.344	1.302	1.449
λ [Å] (Cu or Mo Kα)	0.7107	0.7107	0.7107
μ [mm^{-1}]	0.674	0.489	0.575
abs correction	numerical	numerical	numerical
$F(000)$	3491	908	1688
θ range [deg]	3.46−32.80	2.97−29.14	2.88−29.20
reflns collected	268 199	35 371	42 291
indep reflns	29 874 (R_{Int} = 0.1332)	10 555 (R_{Int} = 0.0355)	9159 (R_{Int} = 0.0329)
T_min/max	0.723/0.962	0.834/0.941	0.922/0.958
data/restr/param	29 874/84/1111	10 555/40/563	9159/0/534
GOF on F^2	1.022	1.037	1.047
R1[a]/wR2[b] [$I > 2\sigma(I)$]	0.1005/0.2599	0.0663/0.1963	0.0476/0.1128
R1/wR2 (all data)	0.1939/0.2906	0.0814/0.2108	0.0592/0.1201
peak/hole/e·Å^{-3}	1.930/−0.843	1.821/−0.780	0.747/−0.792

[a] $R1 = \sum||F_o| - |F_c||/\sum|F_o|$. [b] $wR2 = [\sum w(|F_o| - |F_c|)^2/\sum w|F_o|^2]^{1/2}$.

sh (77), 872 (123). Crystals suitable for single-crystal X-ray diffraction were grown by layering a CH_2Cl_2 solution with MeOH and allowing solvents to diffuse. Analysis of the original methanol insoluble solid that was isolated by suction filtration, washing with Et_2O, and then air-drying was consistent with **1**·0.5 H_2O. Anal. Calcd for $C_{40}H_{37}N_{10}NiO_{0.5}$: C, 66.31; H, 5.15; N, 19.33. Found: C, 66.07; H, 5.16; N, 19.15.

Chemical Oxidations. *$[Ni(Me,Me)_2](BF_4)_2$, $(1)(BF_4)_2$.* A solution of 0.128 g (0.468 mmol) of $FcBF_4$ in 10 mL of CH_2Cl_2 was added to a solution of 0.168 g (0.234 mmol) of **1** in 20 mL of CH_2Cl_2. To ensure quantitative transfer, the flask originally containing the ferrocenium solution was washed with an additional 5 mL of CH_2Cl_2 solution, and the washings were transferred via cannula to the reaction mixture. After the resulting violet solution had been stirred 30 min at room temperature, solvent was removed under vacuum. The violet solid was washed sequentially with four 10 mL portions of toluene, two 10 mL portions of Et_2O, and then was dried by heating at 80 °C under vacuum for 4 h to leave 0.194 g (89%) of $(1)(BF_4)_2 \cdot 0.5CH_2Cl_2$ as a violet solid. Mp, >350 °C. Anal. Calcd for $C_{40.5}H_{37}B_2ClF_8N_{10}Ni$: C, 52.22; H, 4.00; N, 15.04. Found: C, 52.56; H, 4.33; N, 14.68. μ_{eff} (solid, 295 K) = 4.7 μ_B. UV−vis (CH_2Cl_2) λ_{max}, nm (ε, M^{-1}, cm^{-1}): 316 (16 900), 364 (22 340), 527 (6150), 609 (3640), 761 (18 100), 1136 (160). X-ray quality crystals of $(1)(BF_4)_2 \cdot 2CH_2Cl_2$ were grown by layering hexanes over a CH_2Cl_2 solution and allowing solvents to diffuse over 20 h.

$[Ni(Me,Me)_2](BF_4) \cdot 0.5CH_2Cl_2$, $(1)(BF_4) \cdot 0.5CH_2Cl_2$. Under an argon atmosphere, a solution of 0.106 g (0.114 mmol) of $(1)(BF_4)_2 \cdot 0.5CH_2Cl_2$ in 10 mL of CH_2Cl_2 was added via cannula transfer to a solution of 0.0815 g (0.114 mmol) of **1** in 10 mL of CH_2Cl_2. After the resulting blue-violet solution had been stirred 30 min at room temperature, solvent was removed under vacuum and then was dried at room temperature under vacuum for 12 h to leave 0.160 g (84%) of a blue-violet solid that was analyzed as $(1)(BF_4) \cdot 0.5CH_2Cl_2$. Mp, >350 °C. Anal. Calcd for $C_{40.5}H_{37}BClF_4N_{10}Ni$: C, 57.31; H, 4.39; N, 16.50. Found: C, 57.25; H, 4.55; N, 16.44. μ_{eff} (solid, 295 K) = 3.7 μ_B. UV−vis (CH_2Cl_2) λ_{max}, nm (ε, M^{-1}, cm^{-1}): 348 (22 600), 402 sh (10 800), 509 sh (2100), 580 (2800), 758 (5700), 3003 (1000). An attempt to grow single crystals by layering a CH_2Cl_2 solution with benzene and allowing solvents to diffuse 1 day produced violet needles of $(1)(BF_4)_2 \cdot 2C_6H_6$ by disproportionation

Crystallography. X-ray intensity data from a brown prism of **1**, a brown needle of $3 \cdot CH_2Cl_2$, a brown plate of **4**, a red block of **6**, a brown needle of $8 \cdot 1.29CH_2Cl_2$, a brown block of **10**·2acetone, a red prism of **10**·acetone, a violet needle of $[Ni(Me,Me)_2](BF_4)_2 \cdot 2CH_2Cl_2$, $(1)(BF_4)_2 \cdot 2CH_2Cl_2$, and a violet needle of $(1)(BF_4)_2 \cdot 2C_6H_6$ were collected at 100.0(1) K with an Oxford Diffraction Ltd. Supernova diffractometer equipped with a 135 mm Atlas CCD detector using Mo(Kα) radiation for $8 \cdot 1.29$ and both solvates of **10** but using Cu(Kα) for the other experiments. Raw data frame integration and Lp corrections were performed with either CrysAlis Pro (Oxford Diffraction, Ltd.)[20] or SAINT+ (Bruker).[21] Final unit cell parameters were determined by least-squares refinement of 9389, 28 800, 6900, 9976, 51 210, 15 532, 18 121, 15 224, and 8870 reflections of **1**, $3 \cdot CH_2Cl_2$, **4**, **6**, $8 \cdot 1.29CH_2Cl_2$, **10**·2acetone, **10**·acetone, $(1)(BF_4)_2 \cdot 2CH_2Cl_2$, and $(1)(BF_4)_2 \cdot 2C_6H_6$, respectively, with $I > 2\sigma(I)$ for each. Analysis of the data showed negligible crystal decay during collection in each case. Direct methods, structure solutions, difference Fourier calculations, and full-matrix least-squares refinements against F^2 were performed with SHELXTL.[22] An empirical absorption correction using spherical harmonics, implemented in the SCALE3 ABSPACK[23] scaling algorithm, was applied to the data for $3 \cdot CH_2Cl_2$, while numerical absorption corrections based on Gaussian integration over a multifaceted crystal model were applied to the data for the remaining crystals. All non-hydrogen atoms were refined with anisotropic

dx.doi.org/10.1021/ic500657e | Inorg. Chem. 2014, 53, 10070−10084

displacement parameters. Hydrogen atoms were placed in geometrically idealized positions and included as riding atoms. The X-ray crystallographic parameters and further details of data collection and structure refinements are given in Tables 1−3.

Table 3. Crystallographic Data Collection and Structure Refinement for $[Ni(Me,Me)_2](BF_4)_2{\cdot}2CH_2Cl_2$, $(1)(BF_4)_2{\cdot}2CH_2Cl_2$, and $[Ni(Me,Me)_2](BF_4)_2{\cdot}2C_6H_6$, $(1)(BF_4)_2{\cdot}2C_6H_6$

	compound	
	$(1)(BF_4)_2{\cdot}2CH_2Cl_2$	$(1)(BF_4)_2{\cdot}2C_6H_6$
formula	$C_{42}H_{40}B_2Cl_4F_8N_{10}Ni$	$C_{52}H_{48}B_2F_8N_{10}Ni$
formula weight	1058.97	1045.33
crystal system	monoclinic	monoclinic
space group	$P2_1/c$	Cc
temp [K]	100.0(1)	100.0(1)
a [Å]	24.8291(6)	9.2835(2)
b [Å]	9.5433(2)	25.5403(7)
c [Å]	20.5730(5)	20.4839(6)
α [deg]	90.00	90.00
β [deg]	108.734(3)	98.748(3)
γ [deg]	90.00	90.00
V [Å^3]	4616.52(19)	4800.3(2)
Z	4	4
D_{calcd} [g cm^{-3}]	1.524	1.446
λ [Å] (Cu Kα)	1.5418	1.5418
μ [mm^{-1}]	3.407	1.272
abs correction	numerical	numerical
$F(000)$	2160	2160
θ range [deg]	3.76−73.76	4.09−73.78
reflns collected	38 581	17 439
indep reflns	9154 (R_{Int} = 0.0336)	8984 (R_{Int} = 0.0447)
T_min/max	0.336/0.868	0.738/0.962
data/restr/param	9154/0/608	8984/2/662
GOF on F^2	1.049	1.037
R1[a]/wR2[b] [$I > 2\sigma(I)$]	0.0639/0.1830	0.0596/0.1618
R1/wR2 (all data)	0.0732/0.1949	0.0632/0.1672
peak/hole/e·Å^{-3}	1.254/−0.809	1.254/−0.809

[a] $R1 = \sum||F_o| - |F_c||/\sum|F_o|$. [b] $wR2 = [\sum w(|F_o| - |F_c|)^2/\sum w|F_o|^2]^{1/2}$.

RESULTS AND DISCUSSION

Eight new and four known[19] NNN-pincer ligands, H(X,Y), with pyrazolyl flanking donors attached to diarylamine anchors with different *para*-aryl (X- and Y-) substituents have been prepared by a variety of synthetic routes as described in the Supporting Information (Schemes S1−S4). The one-pot reaction between $NiCl_2{\cdot}6H_2O$ and 2 mol equiv[24] of each of the 12 H(X,Y) ligands followed by 2 mol equiv of $(NEt_4)(OH)$ in MeOH rapidly afforded precipitates of "$Ni(X,Y)_2$"; the soluble byproducts (H_2O, NEt_4Cl) were removed by filtration. If the precipitates are collected by suction filtration, washed with Et_2O (minimal in the cases of **2**, **9**, and **11**, vide infra), and air-dried, then samples analyze as either hemihydrates, hydrates, a dimethanol solvate (for $Ni(Me,CO_2Et)_2$), or are solvent-free ($Ni(Me,Br)_2$, **4**, and $Ni(Br,Br)_2$, **7**) as detailed in the Experimental Section and Supporting Information. Heating these samples under vacuum over the course of hours is sufficient to remove solvent in seven of the cases (see Scheme 1), but solvent could not be completely removed in the remaining cases. Solvate molecules are retained by complexes with Lewis donor X- or Y-groups and derivatives with hydrogen at the *para*-aryl position. While the former cases are easily understood, the reason why water is retained in the latter cases (**2**·0.5 H_2O and **3**·0.5 H_2O) is not clear, as it has not yet been possible to grow single crystals for X-ray structural studies.[25] The yields shown in Scheme 1 (>80%) correspond to samples after washing and heating under vacuum. The characterization data were acquired from samples that analyzed as shown in Scheme 1. The $Ni(X,Y)_2$ complexes are generally soluble in halogenated solvents, moderately soluble in aromatic solvents, THF, acetone, CH_3CN, and nitromethane, very slightly soluble in alcohols, but insoluble in alkanes and Et_2O. Exceptions occur for $Ni(Me,H)_2{\cdot}0.5\ H_2O$, $Ni(CF_3,CF_3)_2$, and $Ni(^{tBu}Ph,^{tBu}Ph)_2$, which show appreciable solubility in Et_2O. In these cases, the methanol precipitates were washed with either minimal Et_2O or with hexanes to remove any inadvertent excess ligand prior to drying. In contrast, the $Ni(X,Y)_2$ complexes with cyano substituents (**8**, **10**, and **12**) are noticeably less soluble in organic solvents than the other nine derivatives. All complexes appear to be air stable both in the solid state and in solution. Each of the 12 complexes is paramagnetic with a solid-state room-temperature magnetic moment in the range of 2.7−3.2 μ_B, as expected for nickel(II) with a significant spin−orbit coupling contribution to the magnetic moment.[26] The solids are also noticeably thermochromic (see Supporting Information Figure S1). At room temperature, the complexes range in color from brown to yellow-brown to orange-brown to red.

Scheme 1. Preparation of $Ni(X,Y)_2$ Complexes

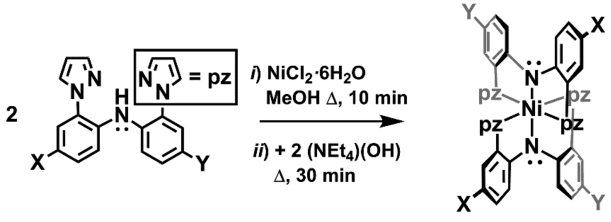

$Ni(Me,Me)_2$ (**1**), 95%
$Ni(Me,H)_2{\cdot}0.5H_2O$ (**2**·0.5H_2O), 87%
$Ni(H,H)_2{\cdot}H_2O$ (**3**·H_2O), 82%
$Ni(Me,Br)_2$ (**4**), 97%
$Ni(Me,CO_2Et)_2{\cdot}2MeOH$ (**5**·2MeOH), 98%
$Ni(Me,CF_3)_2$ (**6**), 97%
$Ni(Br,Br)_2$ (**7**), 85%
$Ni(Me,CN)_2$ (**8**), 88%
$Ni(CF_3,CF_3)_2$ (**9**), 93%
$Ni(CN,CN)_2{\cdot}0.5H_2O$ (**10**·0.5H_2O), 86%
$Ni(^{tBu}Ph,^{tBu}Ph)_2$ (**11**), 95%
$Ni(^{CN}Ph,^{CN}Ph)_2{\cdot}H_2O$ (**12**·H_2O), 88%

dx.doi.org/10.1021/ic500657e | Inorg. Chem. 2014, 53, 10070−10084

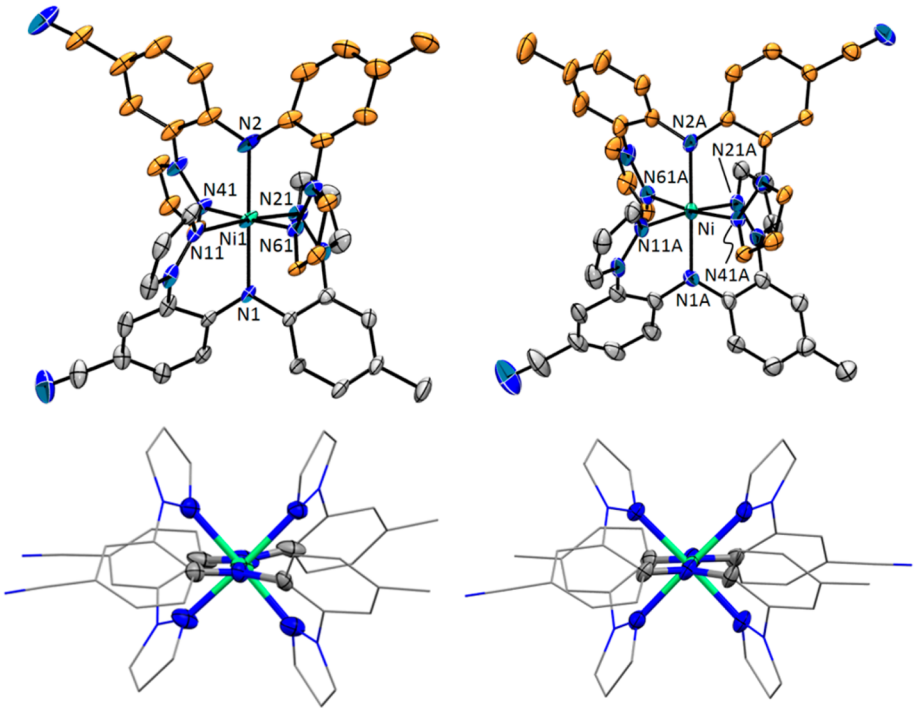

Figure 2. Top: Structures of the two isomers (*cis*-isomer, left; *trans*-isomer, right) of $Ni(Me,CN)_2$ found in the crystal with partial atom labeling. Hydrogen atoms have been removed, and carbon atoms of the top ligand on each complex have been colored gold for clarity. Bottom: Views approximately down N1−Ni−N2 bonds showing the nearly planar amido "$(N_{Ar})_2NiC_4$" moiety.

However, the complexes become bright orange or red (depending on the complex) upon cooling to −196 °C. The origin of the solid-state thermochromic behavior of these $Ni(X,Y)_2$ complexes remains unclear but is likely due to the known temperature dependence of charge transfer bands.[26,27]

The solid-state structures of six $Ni(X,Y)_2$ derivatives have been determined by single-crystal X-ray diffraction. The representative structure of $Ni(Me,CN)_2$ is given in Figure 2, while selected bond distances and angles are given in Table 4; data for other complexes are provided in the Supporting Information (Figures S3−S7). All $Ni(X,Y)_2$ complexes have six-coordinate nickel(II) with an average Ni−N bond distance of 2.07 ± 0.01 Å, in line with other nickel(II) complexes containing NiN_6 kernels.[28] With the exception of *cis*-$Ni(Me,CN)_2$ described later, the nickel center in each complex resides in a compressed octahedral environment where the diarylamido Ni−N_{Ar} bonds are shorter (avg 2.05 ± 0.02 Å) than the pyrazolyl Ni−N_{pz} bonds (avg 2.09 ± 0.02 Å). For asymmetric derivatives $Ni(X,Y)_2$ where X ≠ Y, there are two possible isomers where the X groups are either *cis*- or *trans*- with respect to the central N_{Ar}−Ni−N_{Ar} axis (left and right of Figure 2, respectively). In the case of $Ni(Me,CN)_2$, both isomers are found in a 1:1 ratio as crystallographically independent molecules in the single crystal. The *cis*-$Ni(Me,CN)_2$ isomer differs from all other structurally characterized $Ni(X,Y)_2$ complexes in that the average Ni−N_{Ar} distance of 2.08 ± 0.01 Å is statistically identical to or slightly longer than the average of the Ni−N_{pz} bond distances of 2.07 ± 0.01 Å. For the other structurally characterized asymmetric $Ni(X,Y)_2$ derivatives **4** and **6**, the isomers cocrystallize as (superimposed) disordered pairs (Supporting Information Figure S5). It is also noteworthy that for symmetric derivatives $Ni(X,Y)_2$ where X = Y such as in **1**, **3**, and **10**, the molecules have approximate D_2 symmetry and are chiral. Because of the modest dihedral angle between the mean planes of the pyrazolyl and aryl rings (avg 37 ± 3°), the tridentate ligands are nonplanar. As such, two enantiomers exist that can be differentiated by the relative skew of a line formed by the centroids pyrazolyl rings and a line conjoining centroids of aryl

Table 4. Selected Distances (Å) and Angles (deg) for the Isomers of $Ni(Me,CN)_2$

atom/bond label[a]	*cis*-isomer	*trans*-isomer
Bond Distances (Å)		
Ni1−N1	2.070(4)	2.050(4)
Ni1−N2	2.082(4)	2.057(4)
Ni1−N11	2.073(4)	2.088(4)
Ni1−N21	2.067(4)	2.101(4)
Ni1−N41	2.059(4)	2.082(3)
Ni1−N61	2.084(4)	2.103(4)
Bond Angles (deg)		
N1−Ni1−N2	179.14(15)	178.62(16)
N1−Ni1−N11	86.86(15)	85.80(15)
N1−Ni1−N61	90.54(14)	93.30(15)
N2−Ni1−N61	88.63(15)	87.35(15)
N11−Ni1−N2	92.88(17)	92.97(16)
N11−Ni1−N61	85.91(15)	91.39(15)
N21−Ni1−N1	87.52(15)	86.59(15)
N21−Ni1−N2	92.77(17)	94.66(15)
N21−Ni1−N11	174.22(17)	172.10(15)
N21−Ni1−N61	95.46(15)	86.92(15)
N41−Ni1−N1	92.03(15)	93.14(14)
N41−Ni1−N2	88.79(16)	86.25(14)
N41−Ni1−N11	91.22(16)	90.82(14)
N41−Ni1−N21	87.66(17)	91.72(14)
N41−Ni1−N61	176.04(15)	173.33(15)

[a]Those of *trans*-isomer have an additional "A" after the atom number; thus Ni1−N1 in the *cis*-isomer is Ni1A−N1A in the *trans*-isomer.

dx.doi.org/10.1021/ic500657e | *Inorg. Chem.* 2014, 53, 10070−10084

rings of the same ligand (see Supporting Information Figure S11). Both possible isomers are found in the crystal of each **1**, **3**, and **10**. Similarly, all four isomers of the nominally C_2-symmetric Ni(X,Y)$_2$ complexes **4** and **6** are found in their solid-state structures, as in Supporting Information Figure S12.

It will be useful to examine a qualitative MO diagram of **1** derived from DFT calculations, to facilitate discussion of the electronic properties of the complexes. As detailed in the Experimental Section, a later section, and the Supporting Information, we examined several different theoretical models and all gave qualitatively similar results. Figure 3 provides

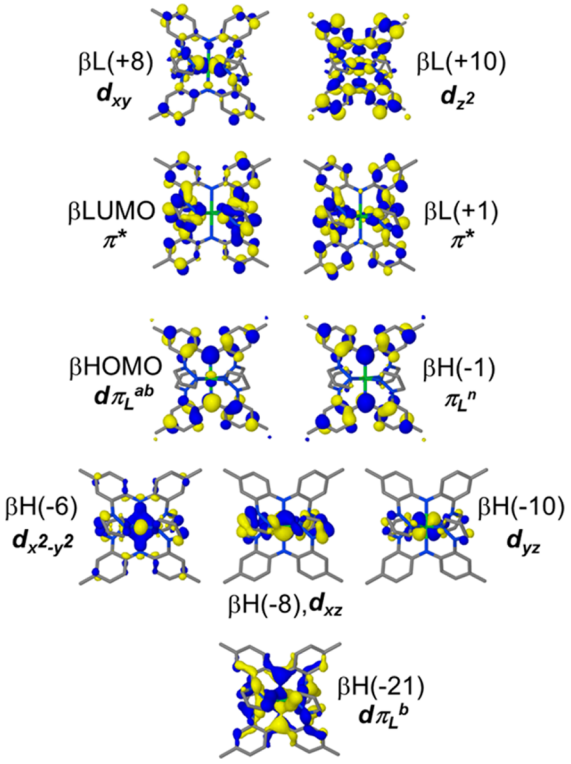

Figure 3. β-Frontier orbitals of Ni(Me,Me)$_2$ calculated at the M06/def2-SV(P) level.

representative "spin-down" β-frontier orbitals of **1** obtained at the M06/def2-SV(P) level of theory. First, each pair of the β-HOMO($-N$) (N = 0, 1) or the β-LUMO($+N$) (N = 0, 1), although not degenerate by symmetry, are essentially energetically degenerate. These four frontier orbitals are mostly ligand-centered with the exception of the β-HOMO that is weakly mixed with a nickel orbital (vide infra). There are two main types of ligand π- (or π^*-) orbitals; those like β-HOMO($-N$) (N = 0, 1) that have significant contributions from the nitrogen p-orbitals and those like β-LUMO($+N$) (N = 0, 1) that do not. We label the former as π_L-orbitals as per Kasha's convention[24] because these presumably involve the electronically active lone pair of electrons on nitrogen, whereas the latter are more conventional π- (or π^*-) orbitals. Second, for simplicity, it is convenient to relabel the axes to swap the usual geometries of the d_{xy} and d_{x2-y2} orbitals. Thus, the z-axis is taken to be coincident with the N_{Ar}–Ni–N_{Ar} vector, while the x- and y-axes bisect *cis*-disposed Ni–N_{py} bonds. As such, the lobes of the d_{xy} orbital are directed along the Ni–N_{py} bonds (β-LUMO(+8), Figure 3) while the lobes of the d_{x2-y2} orbital are between these bonds (β-HOMO(-6), Figure 3). The d_{xz} orbital is then normal to the C_2N_{Ar}Ni planes (with a central amido N_{Ar} atom, see β-HOMO(0, -8, and -21) of Figure 3), and the d_{yz} orbital resides in the C_2N_{Ar}Ni plane (β-HOMO(-10), Figure 3). Thus, the d_{xz} orbital is mainly nonbonding, but there is a small amount of mixing with a π_L-orbital that has out-of-phase nitrogen p_x-orbitals to give a (presumably weak) $d\pi$–$p\pi$ interaction (labeled $d\pi_L^{ab}$ or $d\pi_L^{b}$, in Figure 3, where the superscript describes the antibonding or bonding-type of overlap between the d_{xz} and nitrogen p_x-orbitals). Moreover, the nonbonding d_{yz}, d_{x2-y2}, and d_{xz} orbitals are degenerate (or nearly so depending on the level of theory). The d_{xy} and d_{z2} orbitals are extensively mixed with various π^*-orbitals, but those with highest metal character such as β-LUMO(+8 or +10), Figure 3, are nearly degenerate (by energy considerations) with the latter being slightly higher in energy than the former. Thus, the calculations suggest that despite the low (D_2) symmetry of **1**, the complex behaves electronically like an isolated nickel(II) center in a NiN_6 environment (i.e., with local octahedral symmetry) that only weakly interacts with a ligand π-system. This latter point will be elaborated on in a later section.

Table 5. Summary of d–d, LMCT, and π_L–π^* Bands in the Electronic Absorption Spectra of Ni(X,Y)$_2$ Complexes in CH_2Cl_2

	$\bar{\nu}$, cm^{-1} (ε, M^{-1} cm^{-1})				
compound	$^3A_{2g}\rightarrow{}^3T_{2g}$	$^3A_{2g}\rightarrow{}^3T_{1g}(^3F)$	$^3A_{2g}\rightarrow{}^3T_{1g}(^3P)$[a]	LMCT[b]	π_L–π^*
Ni(Me,Me)$_2$, **1**	11 470 (100)	18 400 (180)	29 800	24 300 (18 000)	27 500 (22 300)
Ni(Me,H)$_2$, **2**[e]	11 520 (110)	18 480 (180)	30 130	24 600 (13 100)	27 400 (31 800)
Ni(H,H)$_2$, **3**[e]	11 510 (110)	18 595 (170)	30 700	25 000 (16 000)	24 900 (14 400)
Ni(Me,Br)$_2$, **4**	11 490 (120)	18 550 (210)	30 560	24 900 (16 100)	27 100 (43 000)
Ni(Me,CO_2Et)$_2$, **5**[e]	11 640 (150)	18 900 (430)[c]	31 530	25 100 (50 100)	25 100 (50 100)
Ni(Me,CF_3)$_2$, **6**	11 500 (100)	18 700 (170)	31 260	25 300 (32 000)	26 500 (36 200)
Ni(Br,Br)$_2$, **7**	11 480 (140)	18 670 (250)	31 210	25 400 (23 000)	26 800 (48 100)
Ni(Me,CN)$_2$, **8**	11 590 (195)[d]	18 800 (380)[c]	31 280	25 800 (57 600)	25 800 (57 600)
Ni(CF_3,CF_3)$_2$, **9**	11 640 (120)[d]	18 900 (210)	31 530	26 700 (45 000)	26 100 (51 500)
Ni(CN,CN)$_2$, **10**[e]	11 600 (170)[d]	na		26 200 (47 000)	24 600 (11 800)
Ni(^{tBu}Ph,^{tBu}Ph)$_2$, **11**	11 520 (240)	na		24 900 (69 900)	24 000 (91 800)
Ni(^{CN}Ph,^{CN}Ph)$_2$, **12**[e]	11 650 (350)	na		25 100 (47 000)	22 000 (11 000)

[a]Estimated from Tanabe–Sugano diagram with C/B = 4.71. [b]Occurring as a shoulder or obtained by deconvolution; ε reported as found in spectrum. [c]From deconvolution of spectra. [d]From the average of split bands. [e]As the solvate shown in Scheme 1. na = not available, masked by intense ligand-based transitions.

dx.doi.org/10.1021/ic500657e | *Inorg. Chem.* 2014, 53, 10070–10084

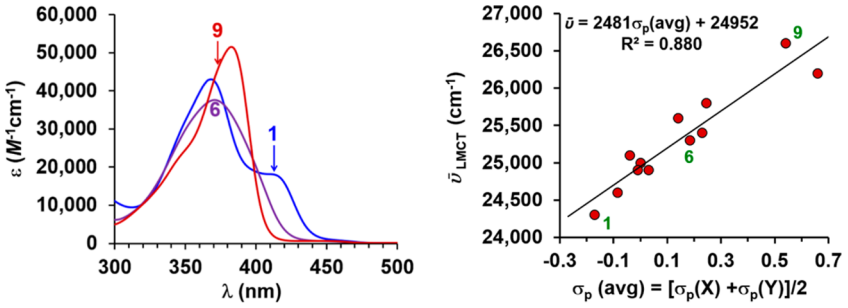

Figure 4. Left: Overlay of higher energy portion of the UV−vis spectrum of **1** (blue), **6** (violet), and **9** (red). Right: Plot showing correlation between energy (cm^{-1}) of LMCT transition and the average of the Hammett σ_p parameter of X and Y *para*-aryl substituents in $Ni(X,Y)_2$ complexes **1**−**12**.

The electronic absorption spectra of **1**−**12** are similar to each other. Exceptions arise from the extended π-systems in **8**, **10**−**12** that shift bands to lower energy (and give higher extinction coefficients) and/or the presence of functional groups in **5**, **8**, **10**, **12** that give more complex bands due to the introduction of added n−π^* transitions. Thus, the spectrum of each compound has two main sets of bands in the visible to NIR region (Table 5). First, there is a set of high intensity (ε > 10 000 M^{-1} cm^{-1}) variably overlapping bands in the higher-energy 300−450 nm range that are due to π_L−π^* and ligand-to-metal charge transfer (LMCT) transitions. Such assignments are based on energy and intensity considerations, by spectral comparisons between series of complexes, and by results of time-dependent density functional (TD-DFT) calculations (Supporting Information). Figure 4 shows an overlay of the higher energy bands for a related series of compounds $Ni(Me,Me)_2$, **1**, $Ni(Me,CF_3)_2$, **6**, and $Ni(CF_3,CF_3)_2$, **9**. The bands in the 325−425 region of the spectra of **1**, **6**, and **9** (and in most other cases) can be deconvoluted into three main Gaussian components: a band invariantly found at 350 nm, a band that progresses from 368 to 384 nm along the series **1** to **6** to **9**, and a band that appears as a shoulder at 413 nm in the spectrum of **1** that shifts to 397 nm in **6**, and to 374 in **9**. The hypsochromic shift of the latter band with increasing electronegativity of the *para*-aryl substituent is a hallmark of a LMCT transition. In fact, the energy of this transition scales linearly with the average of the Hammett σ_p parameters[30] of *para*-aryl substituents (X and Y) in $Ni(X,Y)_2$ complexes, right of Figure 4. TD-DFT calculations suggest the LMCT transitions in this region are between the ligand's π_L^n-orbital (the superscript "n" refers to an in-phase combination of nitrogen p-orbitals on a π_L orbital that is nonbonding by symmetry with respect to any metal d-orbital) and orbitals with significant d_{z2} or d_{xy} character similar to β-LUMO(+8 or +10), Figure 3. The slight bathochromic shift of the middle band in the spectra along the series **1**, **6**, and **9** is suggestive of some MLCT character. TD-DFT calculations suggest that this band is indeed due to an admixture of $d\pi_L^{ab}$−π^* (the $d\pi_L^{ab}$ has some metal character) and π_L^n−π^* transitions, while the invariant band component is an admixture of ligand-based π_L^n−π^* and π−π^* transitions. As exemplified by the overlay of spectra for **1**, **6**, and **9** in the left of Figure 5 and as collected in Table 5, the second common set of bands in the spectra of **1**−**12** are lower-energy bands that are of similar shape and occur in the normal range (500 nm < λ_{max} < 1000 nm) for d−d transitions of many other nickel(II) complexes with NiN_6 coordination.[31] The relatively high intensity ($\varepsilon \approx$ 100−400 M^{-1} cm^{-1}) of these lower energy bands as compared to typical d−d bands ($\varepsilon \approx$ 1−100 M^{-1} cm^{-1}) is suggestive of partial charge transfer character.

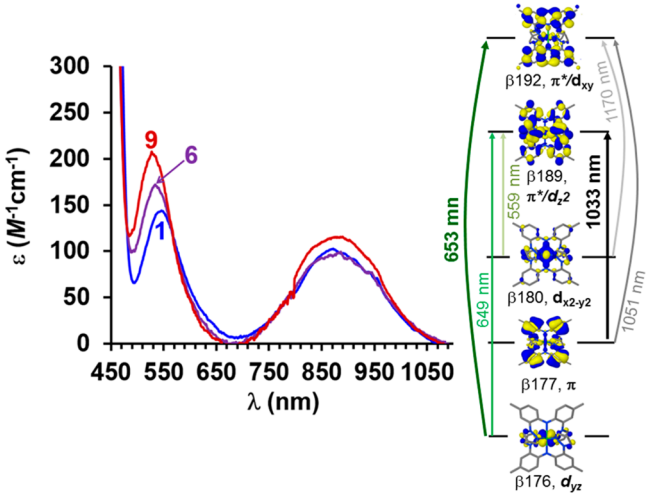

Figure 5. Left: Overlay of the lower energy portion of the UV−vis spectrum of **1** (blue), **6** (violet), and **9** (red) in CH_2Cl_2. Right: Summary of results of TD-DFT calculations (M06/def2-SV(P)) for **1**.

TD-DFT calculations of **1** (right of Figure 5 and Supporting Information Table S5) support the assertion of partial charge transfer character in these bands. For instance, the lowest energy band is calculated to be the sum of three excitations (at 1033, 1051, and 1170 nm) that are each complex admixtures of transitions involving chiefly the five orbitals in the right of Figure 5. The calculated excitation at 1033 nm has the highest oscillator strength of the three components and is bolded most strongly in Figure 5. If one only considers the dominant transition (which is at best 25−50% of the total character) of each excitation, the main component of that at the 1030 or 1051 nm excitation is essentially a π−π^* transition where the π^* has significant metal character from d_{z2} and d_{xy} orbitals. The third excitation calculated at 1170 nm originates from a nearly pure metal orbital (d_{x2-y2}) to a π^* orbital with partial d_{xy} character. The less dominant transitions of the three excitations occur between orbitals with a diverse range of d-, π-, π_L-, or π^*-character. Finally, as with most other nickel(II) complexes with distorted NiN_6 kernels, it is possible to evaluate the ligand field strength from the energy of the d−d bands with the aid of Tanabe−Sugano diagrams because the electronic effects arising from distortion from octahedral symmetry are generally small or negligible in room-temperature solution, especially for weaker-field ligands.[31] Notably the 12 current $Ni(X,Y)_2$ complexes have a nearly constant 10Dq value of 11 480(60) cm^{-1}, which is comparable to that found for nickel(II) complexes of other pyrazolyl-based ligands such as the

dx.doi.org/10.1021/ic500657e | Inorg. Chem. 2014, 53, 10070−10084

tris(pyrazolyl)borates: $Ni(Tp)_2$ (10Dq = 11 900 cm^{-1}), Ni(Tp*= tris(3,5-dimethylpyrazolyl)borate)$_2$ (10Dq = 11 400 cm^{-1}), or $[Ni(Tpm^*$ = tris(3,5-dimethylpyrazolyl)-methane$)_2]^{2+}$ (10Dq = 11 700 cm^{-1}).[32] Importantly, the constant value of 10Dq regardless of ligand substitution in these complexes reflects the weakness of any $d\pi-p\pi$ interactions, in accord with the theoretical calculations.

The electrochemical properties of the 12 $Ni(X,Y)_2$ complexes in dichloromethane solution were measured by cyclic voltammetry. A representative set of voltammograms for **1** in CH_2Cl_2 is given in Figure 6, and a summary of results is given in Table 6. Each complex exhibits two one-electron oxidation waves as assessed by comparisons of current intensities with equimolar solutions of ferrocene and by spectrophotometric titrations with various oxidants. With the exception of $Ni(CN,CN)_2{\cdot}H_2O$, the oxidation waves were quasi-reversible because the ratios of current peak intensities were unity, but the separation between anodic and cathodic peaks was greater than 59 mV and increased with scan rate (Figure 6). For $Ni(CN,CN)_2{\cdot}H_2O$, **10**·H_2O, the voltammograms showed waves characteristic of adsorption processes, because the cathodic current peaks were unexpectedly large but decreased on increasing scan rate or after addition of a few drops of CH_3CN (Supporting Information Figure S13). As shown in Table 6, the first and second oxidation potentials for $Ni(X,Y)_2$ complexes varied over about 700 mV by simply replacing *para*-aryl ligand substituents. There is a strong linear correlation between the average of the Hammett σ_p parameter of the four *para*-aryl substituents of the $Ni(X,Y)_2$ complexes and either the first or the second oxidation potential (Figure 7) where complexes with electron-donating groups are the easiest to oxidize. Such a trend also provides an indication that there is substantial ligand character to the HOMO in both $Ni(X,Y)_2$ and their mono-oxidized counterparts,[33] a feature corroborated by DFT calculations (vide infra). The linear relationship between oxidation potential and Hammett σ_p parameter was useful for establishing the Hammett parameter for the C_6H_4-4-CN group (σ_p = 0.14 ± 0.03), which, to the best of our knowledge, was unknown. These electrochemical results also parallel those from a recent report by the Heyduk group demonstrating that it was possible to tune the redox potential of tungsten(V) complexes of a trianionic triamido ligand over a 270 mV range by changing groups along the ligand periphery without greatly altering the structures or nitrene transfer reactivity of the complexes.[11a] The separation between the two oxidation potentials of the 12 $Ni(X,Y)_2$ complexes ranges between 200 and about 300 mV. Accordingly, the equilibrium constant for comproportionation (K_{com}, eq 1) varies between 10^4 and 10^6 depending on the complex, but without any obvious trend. Regardless, these values indicate that, on the electrochemical time scale, the mono-oxidized complexes $[Ni(X,Y)_2]^+$ are either Robin–Day class II or are nearing the Robin–Day class II/III borderline of mixed valence species.[34] Because the separation of oxidation waves alone is insufficient to establish the strength of electronic communication (and hence unambiguous assignment of Robin–Day class)[35] since the separation could be due to simple Coulombic effects rather than or in addition to electronic communication via super-exhange or hopping mechanisms, further verification was established by spectroscopic and computational means.

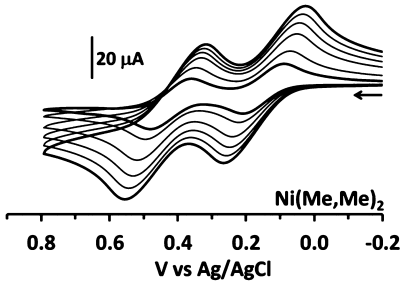

Figure 6. Overlay of cyclic voltammograms of $Ni(Me,Me)_2$ in CH_2Cl_2 obtained at scan rates of 50 (inner), 100, 200, 300, 400, and 500 mV/s (outer).

$$Ni(X,Y)_2 + [Ni(X,Y)_2]^{2+} \rightleftarrows 2[Ni(X,Y)_2]^+$$
$$K_{com} = (M^+)^2/[(M^0)(M^{2+})] \quad (1)$$

The reactions of $Ni(Me,Me)_2$ with ferrocenium tetrafluoroborate, $Fc(BF_4)$, were investigated, as in Scheme 2, to learn more about the properties of the oxidized $[Ni(X,Y)_2]^{n+}$ (n = 1,

Table 6. Electrochemical Data from Cyclic Voltammetry Experiments of 1–12 and Reference Compounds in CH_2Cl_2

	$E^{o\prime}$, V vs Ag/AgCl[a]			
compound	E°_{ox1} ($E_{pa} - E_{pc}$, mV)	E°_{ox2} ($E_{pa} - E_{pc}$, mV)	K_{com}[b]	σ_p(avg)[30]
$Ni(Me,Me)_2$, **1**	0.146 (188)	0.428 (187)	6.57×10^5	−0.17
$Ni(Me,H)_2$, **2**[d]	0.257 (154)	0.536 (156)	5.84×10^5	−0.085
$Ni(H,H)_2$, **3**[d]	0.311 (187)	0.604 (192)	1.01×10^6	0.0
$Ni(Me,Br)_2$, **4**	0.318 (163)	0.582 (165)	3.24×10^5	0.03
$Ni(Me,CO_2Et)_2$, **5**[d]	0.409 (230)	0.656 (208)	1.66×10^5	0.14
$Ni(Me,CF_3)_2$, **6**	0.464 (174)	0.724 (173)	2.77×10^5	0.185
$Ni(Br,Br)_2$, **7**	0.500 (161)	0.751 (153)	1.94×10^5	0.23
$Ni(Me,CN)_2$, **8**	0.584 (175)	0.810 (176)	7.26×10^4	0.245
$Ni(CF_3,CF_3)_2$, **9**	0.763 (170)	1.019 (168)	2.36×10^5	0.54
$Ni(CN,CN)_2$, **10**[d]	0.882 (232)	1.085 (208)	2.94×10^4	0.66
$Ni(^{tBu}Ph,^{tBu}Ph)_2$, **11**	0.274 (136)	0.524 (138)	1.87×10^5	0.01
$Ni(^{CN}Ph,^{CN}Ph)_2$, **12**[d]	0.455 (153)	0.657 (151)	2.82×10^4	0.14[c]
$[Ga(Me,Me)_2]^{+c}$,[19a]	1.165 (207)	0.977(223)	1.62×10^3	−0.17
ferrocene	0.522 (180)			

[a]Average values of $(E_{pa} + E_{pc})/2$ obtained for scan rates of 50, 100, 200, 300, 400, and 500 mV/s with 0.1 M NBu_4PF_6 as supporting electrolyte. [b]$K_{com} = e^{(\Delta E \cdot F/RT)}$, T = 295 K. [c]From this work. [d]As the solvate listed in Scheme 1.

dx.doi.org/10.1021/ic500657e | Inorg. Chem. 2014, 53, 10070–10084

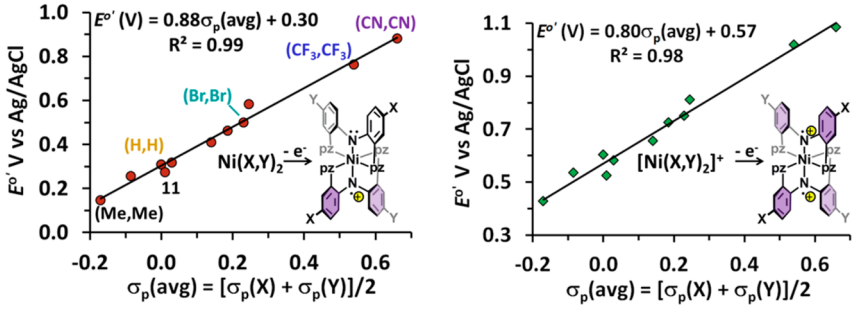

Figure 7. Correlations between oxidation potentials and the average of the Hammett σ_p parameter of *para*-substituents of aryl groups in $Ni(X,Y)_2$ complexes.

Scheme 2. Preparation of Oxidized $[Ni(Me,Me)_2]^{n+}$ (n = 1, 2) Complexes

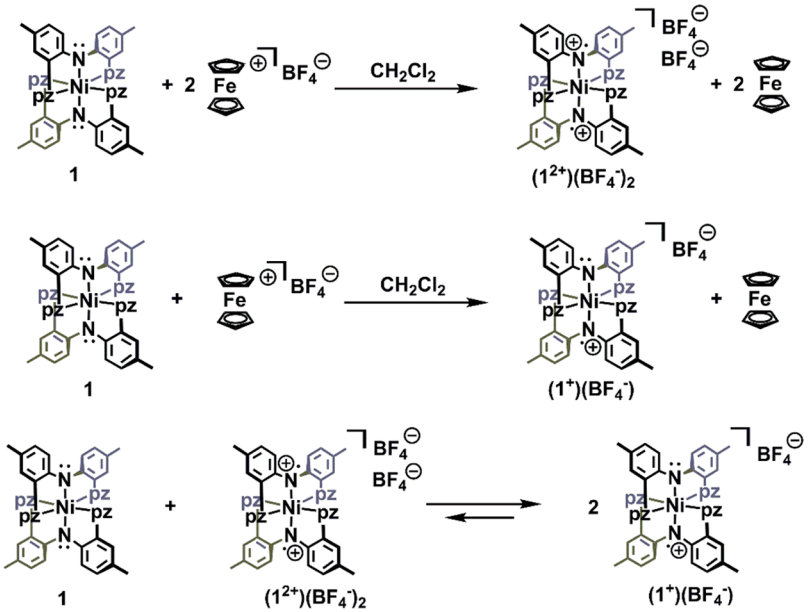

2) complexes. The oxidation potentials of $Ni(Me,Me)_2$, **1** (0.15, 0.43 V vs Ag/AgCl), are sufficiently low to permit two-electron oxidation with the ferrocenium ion, Fc^+ (0.52 V vs Ag/AgCl). Thus, titrations monitored by UV−visible spectroscopy showed that the violet dioxidized complex $[Ni(Me,Me)_2](BF_4)_2$, $(\mathbf{1})(BF_4)_2$, was quantitatively formed in solution by the reaction of **1** with 2 equiv of $FcBF_4$ in dichloromethane, as in the top of Scheme 2. On a preparative scale, the sample crystallizes with 2 equiv of CH_2Cl_2 (vide infra), but loses some solvent on drying under vacuum to give a species that analyzes as $(\mathbf{1})(BF_4)_2{\cdot}0.5CH_2Cl_2$. Complex $(\mathbf{1})(BF_4)_2$, prepared in situ or synthetically as the solvate, is stable in air as a solid or as a solution in CH_2Cl_2 or CH_3CN, but slowly decomposes over the course of hours in THF or propylene carbonate. The solid-state structures of two solvates of $(\mathbf{1})(BF_4)_2$ were determined by single-crystal X-ray diffraction (Supporting Information Figures S8, S9). A comparison of bond distances in the solvates with those in charge-neutral **1** shows two main structural differences. First, the average Ni−N distance in $(\mathbf{1})^{2+}$ is 0.02 Å shorter than that in **1**. This effect is most pronounced in the pyrazolyl groups where the average $Ni-N_{pz}$ distance is 2.065(2) Å in $(\mathbf{1})^{2+}$ but is 2.090(8) Å in **1**. The Ni−N distances involving the aryl amido groups exhibit a lesser or statistically negligible shortening on oxidation; the average $Ni-N_{Ar}$ distance is 2.036(2) Å in $(\mathbf{1})^{2+}$ but is 2.045(7) Å in **1**. This latter observation is opposite of that found for the gallium complexes where oxidation caused a lengthening of the $Ga-N_{Ar}$ bonds (the $Ga-N_{pz}$ bonds shortened upon oxidation, however). A second difference in structures of $(\mathbf{1})^{2+}$ and **1** is manifest in various intraligand C−C and C−N bond distance alterations as well as a decrease in pyrazolyl-aryl dihedral angles on oxidation that are indicative of *ortho*- quinoidal distortions (see Supporting Information Figure S10 and Table S1) similar to those previously observed in the oxidized ligands of $[Ga(Me,Me)_2]^{n+}$ (n = 2,3) complexes.[19a]

The visible spectrum of $(\mathbf{1})(BF_4)_2$ (Supporting Information Figure S14) provides another experimental indicator that oxidation is significantly ligand-centered. The spectrum shows modestly intense ($2000 < \varepsilon < 18\,000$ M^{-1} cm^{-1}) bands in the region of 400−900 nm that are characteristic of π-radical transitions similar to those found in the spectra of mono- and dioxidized $[Ga(Me,Me)_2]^{n+}$ (n = 2,3) complexes, where oxidation is exclusively ligand-based. The lowest energy d−d band was observed for $(\mathbf{1})(BF_4)_2$ (8806 cm^{-1}, ε = 160 M^{-1} cm^{-1}) but was not found in the spectrum of $(\mathbf{1})(BF_4)$ because it was masked by the IVCT band (vide infra). The room-temperature (295 K) solid-state magnetic moment of $(\mathbf{1})(BF_4)_2{\cdot}0.5CH_2Cl_2$, μ_{eff} = 4.7 μ_B, is close to but a little lower than μ_{eff} = 4.9−5.2 μ_B expected for an S = 2 species. In contrast to complex **1**, which was EPR silent, the EPR spectrum of the

dx.doi.org/10.1021/ic500657e | Inorg. Chem. 2014, 53, 10070−10084

dioxidized complex $(\mathbf{1})(BF_4)_2{\cdot}0.5CH_2Cl_2$ in frozen (10 K) CH_2Cl_2 shows a 4*S* signal near $g = 8$ in both perpendicular and parallel modes (Figure 8) indicative of an $S = 2$ spin system.

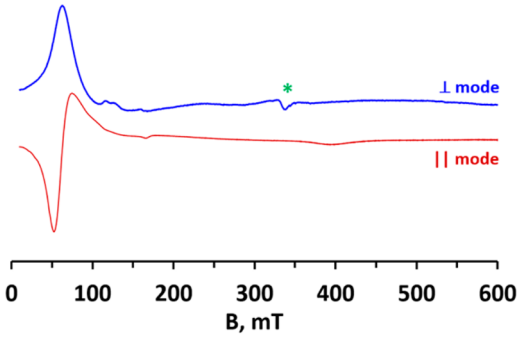

Figure 8. X-band EPR spectrum of $(\mathbf{1})(BF_4)_2{\cdot}0.5CH_2Cl_2$ in frozen (10 K) CH_2Cl_2 acquired in both perpendicular (blue line) and parallel (red line) modes. The signal near 330 mT from a paramagnetic impurity in the sample chamber is demarcated with a green asterisk. Instrumental parameters: parallel mode, freq = 9.387 GHz; power = 10.0 mW, modulation 10 G; perpendicular mode, freq = 9.632 GHz, power = 2.0 mW, modulation 10 G.

While we do not have access to a SQUID magnetometer that would allow for unambiguous assignment of the ground state multiplicity, the $S = 2$ state appears to be significantly populated even at 10 K. Broken-symmetry[36] DFT calculations of $(\mathbf{1})^{2+}$ at the M06-2X/Def2-TZVP level (Supporting Information Table S8) suggest that lower multiplicity states such as the $S = 1$, $[L(\uparrow)-Ni(\uparrow\uparrow)-L(\downarrow)]^{2+}$, and the $S = 0$, $[L(\downarrow)-Ni(\uparrow\uparrow)-L(\downarrow)]^{2+}$, are much higher in energy than the quintet state.

The UV−visible spectrum of $(\mathbf{1})(BF_4)$ (Figure 9) is sufficiently distinct from either **1** or $(\mathbf{1})(BF_4)_2$ to allow spectroscopic monitoring of its formation. UV−visible spectrophotometric titrations show that the blue-violet mono-oxidized complex $(\mathbf{1})(BF_4)$ is formed quantitatively by the comproportionation reaction between **1** and $(\mathbf{1})^{2+}$ in CH_2Cl_2, as in the bottom of Scheme 2. On the synthetic scale, a species that analyzes as $(\mathbf{1})(BF_4){\cdot}0.5CH_2Cl_2$ is isolated from the comproportionation reaction. While UV−visible spectroscopic monitoring indicates that reaction between **1** and 1 equiv of $FcBF_4$ in CH_2Cl_2 affords $(\mathbf{1})(BF_4)$ (as in the middle of Scheme 2), the isolation of pure $(\mathbf{1})(BF_4)$ by this route is complicated by the need to separate ferrocene without disrupting the disproportionation/comproportionation equilibrium. For example, washing the mixture of $(\mathbf{1})(BF_4)$ and ferrocene with toluene or hexanes in an attempt to remove ferrocene also removed some **1** and contaminated the product with $(\mathbf{1})(BF_4)_2$ due to disproportionation (i.e., the reverse reaction in the bottom of Scheme 2). As with the dioxidized derivative, $(\mathbf{1})(BF_4)$ is stable in air as a solid and as solutions in either CH_2Cl_2 or CH_3CN, but solutions in THF or propylene carbonate degrade over the course of hours.

The absorption spectrum of $(\mathbf{1})(BF_4)$ shows medium-intensity bands in the visible region (450−900 nm, left of Figure 9) for π-radical transitions. In addition, a weaker-intensity but broad band is found in the near- to mid-IR region that is absent in the spectrum of either **1** or $(\mathbf{1})(BF_4)_2$. This new band is attributed to the intervalence charge transfer (IVCT) transition, which is expected of a Robin−Day class II or III mixed valence species. Typically, band-shape analysis of the IVCT band is used to obtain information regarding the strength of electronic communication in mixed-valence complexes. In the current case, the limited spectral range of the absorption spectrometer and the difficulties inherent in obtaining molar absorptivity data from IR spectra hinder highly accurate band shape analyses, so an estimate was made by averaging multiple attempts at Gaussian fits of the partial band found in the NIR absorption spectral data. A summary of the data for $(\mathbf{1})(BF_4)$ and the related gallium complex, $[Ga(Me,Me)_2]^{2+}$, is given in Table 7. The use of the Hush relations[37] in eqs 2 and 3 to estimate the electronic coupling element H_{ab} revealed that there is stronger electronic communication between oxidized and nonoxidized ligands in $(\mathbf{1})(BF_4)$ than found for $[Ga(Me,Me)_2](PF_6)(SbCl_6)$, in qualitative agreement with the electrochemical data. In these relations, E_{OP} is the energy of the absorption maximum in cm^{-1}, λ is the Marcus reorganization energy, ε_{max} is the molar extinction coefficient, $\Delta\tilde{\nu}_{1/2}$ is the full-width-at-half-maximum in cm^{-1}, and d is the separation between redox centers in Å. The value of $d = 4.088$ was the nitrogen−nitrogen distance between amido groups found in the geometry-optimized structure of $[Ni(Me,Me)_2]^+$ from DFT calculations (M06/def2-SV(P)) and gives the upper limit for the strength of electronic communication.[38] Spectroscopic evidence in support of the assignment of $(\mathbf{1})(BF_4)$ as a Robin−Day class II mixed valence species includes: (i) the solvent dependence of the IVCT band, as summarized in Table 7; (ii) Gaussian fits of the IVCT band had an experimental $\Delta\tilde{\nu}_{1/2}$ that was larger than the theoretical value[34a,40] $\Delta\tilde{\nu}_{1/2}(HTL) = [16\ \ln(2)k_BT\lambda]^{1/2}$; and (iii) the calculated values of H_{ab} (466 cm^{-1}) and λ (3050) cm^{-1} fall within the accepted limits of $0 < H_{ab} < \lambda/2$ or $0 < 2H_{ab}/\lambda < (1 - [\Delta\tilde{\nu}_{1/2}(HTL)]/2\lambda)$ for class II or class IIA species, respectively.[40] The thermal energy barrier to electron transfer $\Delta G^* = 378$ cm^{-1} calculated using eq 4 from classical Marcus theory[41] is lower than $\Delta G^* = 1344$ cm^{-1} found for the gallium

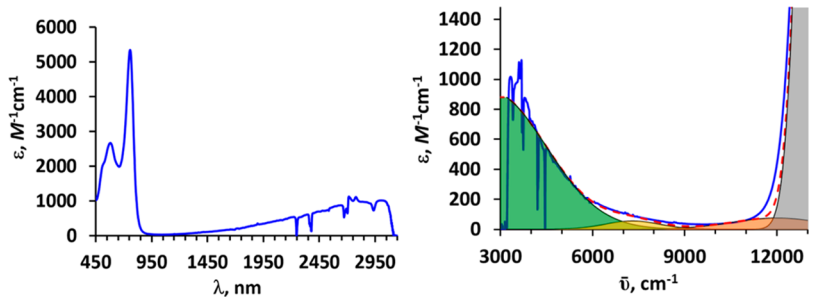

Figure 9. Left: Visible/NIR spectrum of $[Ni(Me,Me)_2]^+$ in CH_2Cl_2. Right: Close-up view of NIR region (in cm^{-1} units) with one attempt at spectral deconvolution shown (Gaussian curves are color-shaded; the sum of curves is the red dashed line).

dx.doi.org/10.1021/ic500657e | Inorg. Chem. 2014, 53, 10070−10084

Table 7. Summary of IVCT Band Shape Fitting and ET Parameters of $(1)(BF_4)$ and $[Ga(Me,Me)_2](PF_6)(SbCl_6)$ in CH_2Cl_2 and CH_3CN

	$(1)(BF_4)$		$[Ga(Me,Me)_2]^{2+b}$	
	CH_2Cl_2[a]	CH_3CN[a]	CH_2Cl_2	CH_3CN
$E_{OP} = \lambda$ (cm^{-1}), eq 2	3050 (173)	3450 (250)	6390	6925
ε_{max} (M^{-1} cm^{-1})	988 (14)	730 (30)	79	55
$\Delta\tilde{\nu}_{1/2}$ (cm^{-1})	2875 (479)	4600 (400)	5192	4900
oscillator strength[c], f_{obs} (f_{calc})	1.3 (2) × 10^{-2}	1.5 (1) × 10^{-2}	1.9 × 10^{-3}	1.2 × 10^{-3}
H_{ab} (cm^{-1}), see eq 3	466 (26)	539 (15)	264	223
$\Delta\tilde{\nu}_{1/2}$ (HTL)[d]	2633 (76)	2800 (100)	3812	3968
$\theta = \Delta\tilde{\nu}_{1/2}/\Delta\tilde{\nu}_{1/2}$ (HTL)	1.1 (2)	1.6 (2)	1.36	1.23
$\alpha = 2H_{ab}/\lambda$	0.30 (2)	0.31 (3)	0.083	0.064
ΔG^* (cm^{-1}), see eq 4	378 (32)	408 (67)	1344	1515
k_{et} (s^{-1}), see eq 5	1.4 (2) × 10^{13}	1.6 (4) × 10^{13}	2.9 × 10^{10}	8.6 × 10^{9}

[a]Standard deviation given in parentheses. [b]See ref 39. [c]$f_{obs} = (4.6 \times 10^{-9})\varepsilon_{max}\Delta\tilde{\nu}_{1/2}$. [d]$\Delta\tilde{\nu}_{1/2}$ (HTL) = $[16\ln(2)k_BT\lambda]^{1/2}$, where k_B = 0.695 cm^{-1} K^{-1} and T = 295 K.

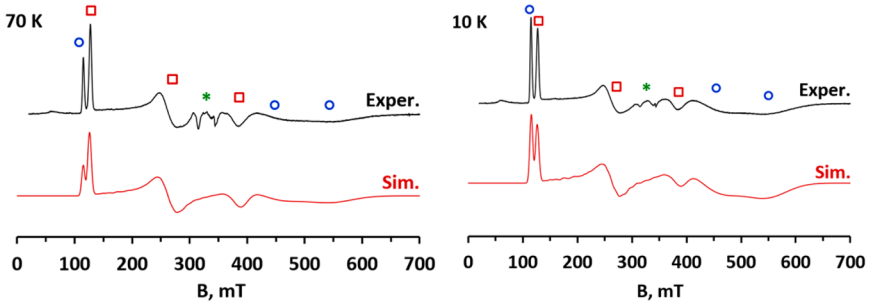

Figure 10. Experimental (black line, top) and simulated (red line, bottom) X-band (9.632 GHz) spectrum of $[Ni(^{tBu}Ph,^{tBu}Ph)_2](BF_4)$ in CH_2Cl_2 at 70 K (left) and 10 K (right). A paramagnetic impurity in the experimental spectra near 330 mT is demarcated with a green asterisk. The simulated spectra were obtained using g_{real} = 2.10; D = 3.34 cm^{-1}, E/D = 0.245, and a D-strain of 0.5 cm^{-1}. Signals due to $m_s = |\pm 3/2\rangle$ and $|\pm 1/2\rangle$ transitions are marked with blue "○" and red "□", respectively. Instrumental parameters: 70 K, power = 5.0 mW, modulation 10 G; 10 K, power = 2.0 mW, modulation 10 G.

complex, which is understandable because it was anticipated that the 3d-orbitals of the nickel center would engage in $d\pi-p\pi$ interactions with the ligand (vide infra), whereas the 3d-orbitals in the gallium complex are expected to be energetically inaccessible. As such, the rate constant for electron transfer, k_{et} = 6.8 × 10^{13} s^{-1}, calculated using eq 5 (where Planck's constant, h = 3.336 × 10^{-11} cm^{-1} s, Boltzmann's constant, k_B = 0.695 cm^{-1} K^{-1}, and T = 295 K) is about 3 orders of magnitude greater in $(1)(BF_4)$ than in $[Ga(Me,Me)_2]^{2+}$.

$$E_{OP} = \lambda \tag{2}$$

$$H_{ab}\ (cm^{-1}) = [(4.2 \times 10^{-4})\varepsilon_{max}\Delta\tilde{\nu}_{1/2}E_{OP}]^{1/2}/d \tag{3}$$

$$\Delta G^* = (\lambda - 2H_{ab})^2/4\lambda\ cm^{-1} \tag{4}$$

$$k_{et} = (2H_{ab}{}^2/h)[\pi^3/\lambda k_B T]^{1/2} \exp - (\Delta G^*/k_B T) \tag{5}$$

The EPR spectra of $(1)(BF_4)$ and $(11)(BF_4)$ in frozen CH_2Cl_2 (10–70 K) were recorded. Each gave a similar rhombic spectra characteristic of an $S = {}^3/_2$ species. The spectra of the latter complex at 70 and 10 K are shown in Figure 10, while the spectrum of $(1)(BF_4)$ is given in the Supporting Information (Figure S15). The spectrum of $(11)(BF_4)$ is a superposition of signals from an $S = {}^3/_2$ species and a small paramagnetic impurity from the sample chamber (green asterisks, Figure 10). The signals from the $S = {}^3/_2$ species were successfully simulated[42] by using g_{real} = 2.10, a zero-field splitting parameter, D, of 3.3 cm^{-1}, and a rhombicity, E/D, of 0.245. The small value of D ensures that the intradoublet transitions of both the $m_s = |\pm 3/2\rangle$ ground state (blue ○, Figure 10) and the $m_s = |\pm 1/2\rangle$ excited state (red □, Figure 10) are populated even at 10 K. Upon warming to 70 K, the signals due to the $m_s = |\pm 1/2\rangle$ component (g_z^{eff} = 1.682, g_y^{eff} = 5.194, g_x^{eff} = 2.488) grow in intensity at the expense of the signals for the $m_s = |\pm 3/2\rangle$ component (g_z^{eff} = 5.682, g_y^{eff} = 1.194, g_x^{eff} = 1.512). Similarly, simulations of the spectra of $(1)(BF_4)$ afforded g_{real} = 2.09, D = 2.3 cm^{-1}, and E/D = 0.236.

To more clearly ascertain the electronic structure of $(1)(BF_4)$, the cation $(1)^+$ was studied computationally. Five salient features arose from the DFT and TD-DFT calculations on $(1)^+$ and comparisons with those on its $[Ni(Me,Me)_2]^{n+}$ (n = 0, 2) relatives. First, the calculated gas-phase structures of **1** and $(1)^{2+}$ produced Ni–N bond distances that were only 0.02 Å longer than those in the solid state, and the experimental structural trend of shortening $Ni-N_{pz}$ distances for dioxidized complexes held for the calculated structures, observations that give confidence to the findings for $(1)^+$. Importantly, because it was not possible to grow single crystals of $[Ni(Me,Me)_2]^+$ for structural studies, the theoretical geometry optimization showed that $(1)^+$ has disparate $Ni-N_{Ar}$ bond distances of 2.063 and 2.025 Å and an estimated $N_{Ar}\cdots N_{Ar}$ distance of 4.088 Å (this latter distance was used in the Hush analysis, vide supra). Moreover, the relative coplanarity of pyrazolyl and aryl rings as well the intraligand bond distances that show *ortho*-quinoidal distortions indicate that the ligand with the longer $Ni-N_{Ar}$ bond was oxidized, whereas the other ligand is not

dx.doi.org/10.1021/ic500657e | Inorg. Chem. 2014, 53, 10070–10084

oxidized. That is, the nonoxidized ligand has an average dihedral angle close to 40°, whereas an oxidized ligand has an average dihedral angle near 30° (Supporting Information Table S4). Also, the *ortho*-quinoidal distortion in an oxidized ligand of $(\mathbf{1})^{+}$ or $(\mathbf{1})^{2+}$ is characterized by shorter C−N_{pz} bonds and a longer C−C bond located between the pyrazolyl and amido nitrogens (Supporting Information Table S4, Figure S17) versus those bonds in an unoxidized ligand. Second, despite the lack of solvated anions, the difference in calculated first- and second-reduction potentials, ΔE^{0}_{calc} = 144 mV (M06-2X/TZVP), associated with the $[Ni(Me,Me)_2]^{n+}$ (n = 0, 1, 2) redox series was aligned with the experimental result, ΔE^{0}_{exp} = 282 mV. Third, the second oxidation is ligand-centered as suggested by the β-HOMO of $(\mathbf{1})^{+}$, which has only small contribution from the metal d_{xz} as shown in the bottom of Figure 11. The

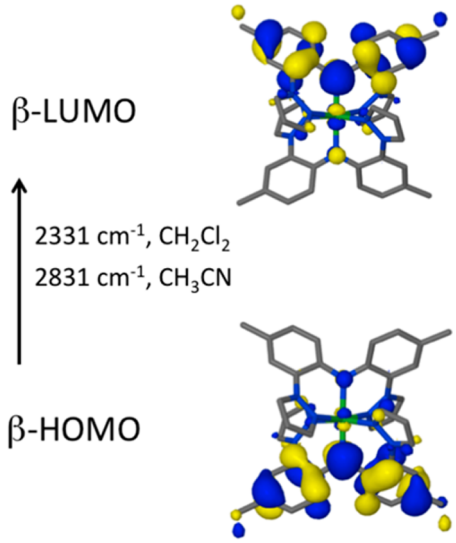

Figure 11. Frontier orbitals of $[Ni(Me,Me)_2]^{+}$ with the calculated energies of the intervalence charge transfer band (TD-DFT, M06/Def2-SV(P)).

lower symmetry of $(\mathbf{1})^{+}$ complicates its MO diagram versus that of **1** or $(\mathbf{1})^{2+}$ because it allows mixing of orbitals that is not permitted by the higher symmetry structures of **1** or $(\mathbf{1})^{2+}$. This point can be illustrated by the β-HOMO of $(\mathbf{1})^{+}$ shown in Figure 11. Here, the orbital is mainly ligand-based and is similar to the π_L^{n} orbital in **1** ((like β-HOMO(−1), Figure 3, with in-phase nitrogen p_x orbitals), but the lobes of the "bottom-half" of the orbital are larger than those in the "top half". The asymmetry the "distorted" π_L^{n} orbital allows some mixing with the d_{xz} orbital to give partial (π-)antibonding character to the N−Ni−N interaction, an interaction that is not allowed by symmetry in **1** or $(\mathbf{1})^{2+}$. The fourth salient point from the calculations then is that the lowest energy electronic excitation of $(\mathbf{1})^{+}$, β-HOMO → β-LUMO, is an intervalence charge transfer transition predicted to be in the NIR to IR region. This transition occurs at an energy that depends on solvent, which is characteristic of a Robin−Day class II species and is fully consistent with the experimental observations. Moreover, several intense (oscillator strength, f > 0.01) β-HOMO(−N) (where $N \geq 1$ and that are essentially aryl-based π orbitals) to β-LUMO ($d\pi_L^{ab}$) electronic (π-radical) transitions are predicted to be found in the far red to green regions of visible region in the spectra of $(\mathbf{1})^{+}$ and $(\mathbf{1})^{2+}$, in accord with experiment. The fifth and final point is that the broken symmetry calculations showed that the quartet state of $(\mathbf{1})^{+}$ was only 1.64 kcal/mol lower in energy than the doublet, [L(↑↓)−Ni(↑↑)−L(↓)]$^{+}$, state. Thermal population of the doublet state may account for the lower than expected magnetic moment of each $(\mathbf{1})^{+}$ and $(\mathbf{11})^{+}$ measured in the solid state at room temperature.

SUMMARY AND CONCLUSIONS

We used four synthetic approaches to prepare eight new and four known pincer-type ligands that have pyrazolyl flanking donors attached to a diarylamine anchor. The 12 pincer variants differ only by the *para*-aryl substituents of the anchor, substituents that dominate the electronic properties of the ligands. As we will report in due course, the synthetic methods reported here are useful because they allow access to a variety of pincer ligands that have different flanking donors and diverse electronic properties. In the current case, we used the 12 ligands to prepare a series of charge-neutral nickel(II) complexes, $Ni(X,Y)_2$, via a simple, high yielding, one-pot reaction that only required filtration for purification of the very poorly soluble desired product. A survey of the electrochemistry of the complexes showed that the first and second oxidation potentials varied linearly over a remarkable 700 mV range with the average of the Hammett σ_p parameters of the ligand's *para*-aryl substituents. Such a finding may be useful for "custom-designing" future reagents for redox-titrations or synthetic single-electron transfer reactions. Importantly, it was found that the oxidation waves were ligand-based regardless of *para*-aryl substituents. This finding was aided by the detailed spectroscopic and computational studies of the singly and doubly oxidized complexes $[Ni(Me,Me)_2]^{n+}$ (n = 1, 2). These studies showed that the unpaired electron(s) on the ligand and those on the nickel center remain essentially uncoupled; the magnetic and EPR spectral data for $[Ni(Me,Me)_2](BF_4)_2$ and $[Ni(Me,Me)_2](BF_4)$ are consistent with S = 2 and S = 3/2 species, respectively. The magnetic orbitals on the oxidized ligands (essentially the amido nitrogen p_x-orbitals directed between molecular axes) are orthogonal to those partly filled orbitals on the metal (d_{z2} and d_{xy} that are directed along the Ni−N_{Ar} bonds), which allows ferromagnetic-type interactions. A comparison of the spectroscopic properties of mono-oxidized complex $[Ni(Me,Me)_2](BF_4)$ and the previously known mono-oxidized gallium(III) complex $[Ga(Me,Me)_2]^{2+}$ afforded insight into the potential role that a bridging metal center can play in mediating electronic communication between its bound unoxidized and oxidized ligands. Such information will be important for making astute decisions about the future design of molecular wires based on covalent or noncovalent assemblies of metal complexes of redox-active pincer complexes. In this vein, the gallium(III) complex $[Ga(Me,Me)_2]^{2+}$ was previously found to be a Robin−Day class II mixed valence species with weak electronic coupling likely occurring via superexchange across the metal bridge facilitated by the energetically accessible empty orbitals. It was originally anticipated that the replacement of gallium with a transition metal would ensure much stronger electronic communication because the metal d-orbitals would allow for dπ−pπ interactions with the ligand's π-system. The electrochemical and spectroscopic studies indeed demonstrated electronic communication exists between oxidized and unoxidized ligands in the mono-oxidized nickel complex $[Ni(Me,Me)_2]^{+}$. However, both the nickel and the gallium complexes are Robin−Day class II(A) mixed valence compounds; the late first-row transition metal only modestly

dx.doi.org/10.1021/ic500657e | *Inorg. Chem.* 2014, 53, 10070−10084

strengthened the communication between ligands as compared to the diamagnetic p-block metal. The theoretical studies revealed that the dπ−pπ interaction in the nickel complex arises from partial mixing of energetically mismatched ligand and (mainly) nonbonding d_{xz} orbitals. It is noted that nickel has the highest spectroscopic electronegativity (1.88 Pauling units) and one of the lowest d-orbital energies (−12.93 eV) of the first-row transition metals.[43] Because the energies of the 3d-orbitals in gallium(III) are expected to be much lower than those in nickel(II), there was no dπ−pπ interaction (β-HOMO, Figure 3). For complexes of the type $[M(Me,Me)_2]^{n+}$, the strength of the dπ−pπ interaction is expected to scale with an increase in d-orbital energies until an energetic match is made with the nearly degenerate set of (noncomplexed) ligand orbitals: the symmetric (nonbonding) combination, π_L^n (like β-HOMO(−1), Figure 3), and its asymmetric counterpart that participates in the dπ−pπ interaction. Better energetic matches with the ligand are expected to occur with the early transition metals, or with second row and third row metals. For such complexes, it is also expected that one electron-oxidation should lead to species that traverse the Robin−Day class II/III border. A future report will detail the effects of replacing metals on the strength of electronic communication and on the relative stability of electronic states in oxidized homoleptic pincer complexes. We will also detail our endeavors at making assemblies from these electroactive units.

■ ASSOCIATED CONTENT

Supporting Information

Experimental and computational details, and crystallographic information files (CIF). This material is available free of charge via the Internet at http://pubs.acs.org.

■ AUTHOR INFORMATION

Corresponding Authors

*Tel.: (414) 456-4787. Fax: (414) 456-6512. E-mail: bbennett@mcw.edu.

*Tel.: (414) 288-3533. Fax: (414) 288-7066. E-mail: james.gardinier@marquette.edu.

Notes

The authors declare no competing financial interest.

■ ACKNOWLEDGMENTS

J.R.G. thanks the NSF (CHE-0848515) for financial support and Prof. J. F. Berry and Prof. Q. Timerghazin for helpful discussions.

■ REFERENCES

(1) (a) Kaim, W. *Eur. J. Inorg. Chem.* **2012**, *3*, 343−348. (b) Caulton, K. G. *Eur. J. Inorg. Chem.* **2012**, *3*, 435−443. (c) Kaim, W. *Inorg. Chem.* **2011**, *50*, 9752−9765. (d) Forum on redox-active Ligands: Kaim, W. *Inorg. Chem.* **2011**, *50*, 9737−9914. (e) Kaim, W.; Schwederski, B. *Coord. Chem. Rev.* **2010**, *254*, 1580−1588.

(2) (a) Ray, K.; Petrenko, T.; Wieghardt, K.; Neese, F. *Dalton Trans.* **2007**, 1552−1566. (b) Hirao, T. *Coord. Chem. Rev.* **2002**, *226*, 81−91. (c) Pierpont, C. G. *Coord. Chem. Rev.* **2001**, *216−217*, 99−125.

(3) (a) Munha, R. F.; Zarkesh, R. A.; Heyduk, A. F. *Dalton Trans.* **2013**, *42*, 3751−3766. (b) Luca, O. R.; Crabtree, R. H. *Chem. Soc. Rev.* **2013**, *42*, 1440−1459. (c) Praneeth, V. K. K.; Ringenberg, M. R.; Ward, T. R. *Angew. Chem., Int. Ed.* **2012**, *51*, 10228−10234. (d) Lyaskovskyy, V.; de Bruin, B. *ACS Catal.* **2012**, *2*, 270−279. (e) Pratt, R. C.; Lyons, C. T.; Wasinger, E. C.; Stack, T. D. P. *J. Am. Chem. Soc.* **2012**, *134*, 7367−7377.

(4) (a) Paul, N. D.; Rana, U.; Goswami, S.; Mondal, T. K.; Goswami, S. *J. Am. Chem. Soc.* **2012**, *134*, 6520−6523. (b) Givaja, G.; Amo-Ochoa, P.; Gómez-García, C. J.; Zamora, F. *Chem. Soc. Rev.* **2012**, *41*, 115−147. (c) Hou, C.; Peng, J.; Xu, Q.; Ji, Z.; Hu, X. *RSC Adv.* **2012**, *2*, 12696−12698 and references. (d) Allendorf, M. D.; Schwartzberg, A.; Stavila, V.; Talin, A. A. *Chem.—Eur. J.* **2011**, *17*, 11372−11388. (e) Evangelio, E.; Ruiz-Molina, D. *Eur. J. Inorg. Chem.* **2005**, *15*, 2957−2971.

(5) For example: (a) Fortier, S.; Le Roy, J. J.; Chen, C.-H.; Vieru, V.; Murugesu, M.; Chibotaru, L. F.; Mindiola, D. J.; Caulton, K. G. *J. Am. Chem. Soc.* **2013**, *135*, 14670−14678. (b) Matson, E. M.; Opperwall, S. R.; Fanwick, P. E.; Bart, S. C. *Inorg. Chem.* **2013**, *52*, 7295−7304. (c) Matsumoto, T.; Chang, H.-C.; Wakizaka, M.; Ueno, S.; Kobayashi, A.; Nakayama, A.; Taketsugu, T.; Kato, M. *J. Am. Chem. Soc.* **2013**, *135*, 8646−8654. (d) Tsvetkov, N. P.; Chen, C.-H.; Andino, J. G.; Lord, R. L.; Pink, M.; Buell, R. W.; Caulton, K. G. *Inorg. Chem.* **2013**, *52*, 9511−9521. (e) Ghosh, P.; Samanta, S.; Roy, S. K.; Joy, S.; Krämer, T.; McGrady, J. E.; Goswami, S. *Inorg. Chem.* **2013**, *52*, 14040−14049 and references. (f) Lippert, C. A.; Riener, K.; Soper, J. D. *Eur. J. Inorg. Chem.* **2012**, *3*, 554−561. (g) Cates, C. D.; Myers, T. W.; Berben, L. A. *Inorg. Chem.* **2012**, *51*, 11891−11897. (h) Ouch, K.; Mashuta, M. S.; Grapperhaus, C. A. *Inorg. Chem.* **2011**, *50*, 9904−9914. (i) Ringenberg, M. R.; Kokatam, S. L.; Heiden, Z. M.; Rauchfuss, T. B. *J. Am. Chem. Soc.* **2008**, *130*, 788−789. (j) Chaudhuri, P.; Wagner, R.; Pieper, U.; Biswas, B.; Weyhermüller, T. *Dalton Trans.* **2008**, 1286−1288. (k) Verani, C. N.; Gallert, S.; Bill, E.; Weyhermüller, T.; Weighardt, K.; Chaudhuri, P. *Chem. Commun.* **1999**, 1747−1748.

(6) (a) Ghosh, P.; Samanta, S.; Roy, S. K.; Demeshko, S.; Meyer, F.; Goswami, S. *Inorg. Chem.* **2014**, *53*, 4678−4686. (b) Fullmer, B. C.; Fan, H.; Pink, M.; Huffman, J. C.; Tsvetkov, N. P.; Caulton, K. G. *J. Am. Chem. Soc.* **2011**, *133*, 2571−2582. (c) He, T.; Tsvetkov, N. P.; Andino, J. G.; Gao, X.; Fullmer, B. C.; Caulton, K. G. *J. Am. Chem. Soc.* **2010**, *132*, 910−911. (d) Rimmer, R. D.; Grills, D. C.; Fan, H.; Ford, P. C.; Caulton, K. G. *J. Am. Chem. Soc.* **2007**, *129*, 15430−15431.

(7) (a) Hojilla Atienza, C. C.; Milsmann, C.; Semproni, S. P.; Turner, Z. R.; Chirik, P. J. *Inorg. Chem.* **2013**, *52*, 5403−5417. (b) Tondreau, A. M.; Stieber, S. C. E.; Milsmann, C.; Lobkovsky, E.; Weyhermuller, T.; Semproni, S. P.; Chirik, P. J. *Inorg. Chem.* **2013**, *52*, 635−646. (c) Darmon, J. M.; Stieber, S. C. E.; Sylvester, K. T.; Fernandez, I.; Lobkovsky, E.; Semproni, S. P.; Bill, E.; Wieghardt, K.; DeBeer, S.; Chirik, P. J. *J. Am. Chem. Soc.* **2012**, *134*, 17125−17137. (d) Russell, S. K.; Bowman, A. C.; Lobkovsky, E.; Wieghardt, K.; Chirik, P. J. *Eur. J. Inorg. Chem.* **2012**, *2012*, 535−545. (e) Russell, S. K.; Milsmann, C.; Lobkovsky, E.; Weyhermuller, T.; Chirik, P. J. *Inorg. Chem.* **2011**, *50*, 3159−3169. (f) Bowman, A. C.; Milsmann, C.; Bill, E.; Lobkovsky, E.; Weyhermuller, T.; Wieghardt, K.; Chirik, P. J. *Inorg. Chem.* **2010**, *49*, 6110−6123. (g) Bowman, A. C.; Milsmann, C.; Hojilla Atienza, C. C.; Lobkovsky, E.; Wieghardt, K.; Chirik, P. J. *J. Am. Chem. Soc.* **2010**, *132*, 1676−1684.

(8) (a) Mossin, S.; Tran, B. L.; Adhikari, D.; Pink, M.; Heinemann, F. W.; Sutter, J.; Szilagyi, R. K.; Meyer, K.; Mindiola, D. J. *J. Am. Chem. Soc.* **2012**, *134*, 13651−13661. (b) Kilgore, U. J.; Sengelaub, C. A.; Fan, H.; Tomaszewski, J.; Karty, J. A.; Baik, M.-H.; Mindiola, D. J. *Organometallics* **2009**, *28*, 843−852. (c) Adhikari, D.; Mossin, S.; Basuli, F.; Dible, B. R.; Chipara, M.; Fan, H.; Huffman, J. C.; Meyer, K.; Mindiola, D. J. *Inorg. Chem.* **2008**, *47*, 10479−10490. (d) Adhikari, D.; Mossin, S.; Basuli, F.; Huffman, J. C.; Szilagyi, R. K.; Meyer, K.; Mindiola, D. J. *J. Am. Chem. Soc.* **2008**, *130*, 3676−3682. (e) Fafard, C. M.; Adhikari, D.; Foxman, B. M.; Mindiola, D. J.; Ozerov, O. V. *J. Am. Chem. Soc.* **2007**, *129*, 10318−10319.

(9) (a) Smith, D. A.; Herbert, D. E.; Walensky, J. R.; Ozerov, O. V. *Organometallics* **2013**, *32*, 2050−2058. (b) Bacciu, D.; Chen, C.-H.; Surawatanawong, P.; Foxman, B. M.; Ozerov, O. V. *Inorg. Chem.* **2010**, *49*, 5328−5334. (c) Radosevich, A. T.; Melnick, J. G.; Stoian, S. A.; Bacciu, D.; Chen, C.-H.; Foxman, B. M.; Ozerov, O. V.; Nocera, D. G. *Inorg. Chem.* **2009**, *48*, 9214−9221.

(10) (a) Klein, A.; Vicic, D. A.; Biewer, C.; Kieltsch, I.; Stirnat, K.; Hamacher, C. *Organometallics* **2012**, *31*, 5334−5341. (b) Madhira, V.

N.; Ren, P.; Vechorkin, O.; Hu, X.; Vicic, D. A. *Dalton Trans.* **2012**, *41*, 7915−7919. (c) Kieltsch, I.; Dubinina, G. G.; Hamacher, C.; Kaiser, A.; Torres-Nieto, J.; Hutchison, J. M.; Klein, A.; Budnikova, Y.; Vicic, D. A. *Organometallics* **2010**, *29*, 1451−1456.

(11) (a) Munha, R. F.; Zarkesh, R. A.; Heyduk, A. F. *Inorg. Chem.* **2013**, *52*, 635−646. (b) Wong, J. L.; Sanchez, R. H.; Logan, J. G.; Zarkesh, R. A.; Ziller, J. W.; Heyduk, A. F. *Chem. Sci.* **2013**, *4*, 1906−1910. (c) Shaffer, D. W.; Szigethy, G.; Ziller, J. W.; Heyduk, A. F. *Inorg. Chem.* **2013**, *52*, 2110−2118. (d) Szigethy, G.; Heyduk, A. F. *Dalton Trans.* **2012**, *41*, 8144−8152. (e) Szigethy, G.; Shaffer, D. W.; Heyduk, A. F. *Inorg. Chem.* **2012**, *51*, 12606−12618. (f) Lu, F.; Zarkesh, R. A.; Heyduk, A. F. *Eur. J. Inorg. Chem.* **2012**, *2012*, 467−470. (g) Heyduk, A. F.; Zarkesh, R. A.; Nguyen, A. I. *Inorg. Chem.* **2011**, *50*, 9849−9863. (h) Nguyen, A. I.; Blackmore, K. J.; Carter, S. M.; Zarkesh, R. A.; Heyduk, A. F. *J. Am. Chem. Soc.* **2009**, *131*, 3307−3316.

(12) (a) Breitenfeld, J.; Ruiz, J.; Wodrich, M. D.; Hu, X. *J. Am. Chem. Soc.* **2013**, *135*, 12004−12012. (b) Breitenfeld, J.; Scopelliti, R.; Hu, X. *Organometallics* **2012**, *31*, 2128−2136. (c) Breitenfeld, J.; Vechorkin, O.; Corminboeuf, C.; Scopelliti, R.; Hu, X. *Organometallics* **2010**, *29*, 3686−3689. (d) Vechorkin, O.; Csok, Z.; Scopelliti, R.; Hu, X. L. *Chem.—Eur. J.* **2009**, *15*, 3889−3899. (e) Vechorkin, O.; Hu, X. L. *Angew. Chem., Int. Ed.* **2009**, *48*, 2937−2940. (f) Csok, Z.; Vechorkin, O.; Harkins, S. B.; Scopelliti, R.; Hu, X. *J. Am. Chem. Soc.* **2008**, *130*, 8156−8157.

(13) Wright, D. D.; Brown, S. N. *Inorg. Chem.* **2013**, *52*, 7831−7833.

(14) Myers, T. W.; Berben, L. A. *J. Am. Chem. Soc.* **2013**, *135*, 9988−9990.

(15) (a) Frazier, B. A.; Williams, V. A.; Wolczanski, P. T.; Bart, S. C.; Meyer, K.; Cundari, T. R.; Lobkovsky, E. B. *Inorg. Chem.* **2013**, *52*, 3295−3312. (b) Frazier, B. A.; Bartholomew, E. R.; Wolczanski, P. T.; DeBeer, S.; Santiago-Berrios, M.; Abruña, H. D.; Lobkovsky, E. B.; Bart, S. C.; Mossin, S.; Meyer, K.; Cundari, T. R. *Inorg. Chem.* **2011**, *50*, 12414−12436.

(16) (a) Gloaguen, Y.; Jacobs, W.; de Bruin, B.; Lutz, M.; van der Vlugt, J. I. *Inorg. Chem.* **2013**, *52*, 1682−1684. (b) Tejel, C.; Ciriano, M. A.; del Río, M. P.; van den Bruele, F. J.; Hetterscheid, D. G. H.; i Spithas, N. T.; de Bruin, B. *J. Am. Chem. Soc.* **2008**, *130*, 5844−5845. (c) Hetterscheid, D. G. H.; Klop, M.; Kicken, R. J. N. A. M.; Smits, J. M. M.; Reijerse, E. J.; de Bruin, B. *Chem.—Eur. J.* **2007**, *13*, 3386−3405.

(17) (a) Puschmann, F. F.; Harmer, J.; Stein, D.; Rüegger, H.; de Bruin, B.; Grützmacher, H. *Angew. Chem., Int. Ed.* **2009**, *49*, 385−389. (b) Büttner, T.; Geier, J.; Frison, G.; Harmer, J.; Calle, C.; Schweiger, A.; Schönberg, H.; Grützmacher, H. *Science* **2005**, *307*, 235−238.

(18) Niwa, T.; Nakada, M. *J. Am. Chem. Soc.* **2012**, *134*, 13538−13541.

(19) (a) Liddle, B. J.; Wanniarachchi, S.; Hewage, J. S.; Lindeman, S. V.; Bennett, B.; Gardinier, J. R. *Inorg. Chem.* **2012**, *51*, 12720−12728. (b) Wanniarachchi, S.; Liddle, B. J.; Kizer, B.; Hewage, J. S.; Lindeman, S. V.; Gardinier, J. R. *Inorg. Chem.* **2012**, *51*, 10572−10580. (c) Wanniarachchi, S.; Liddle, B. J.; Lindeman, S. V.; Gardinier, J. R. *J. Organomet. Chem.* **2011**, *696*, 3623−3636. (d) Wanniarachchi, S.; Liddle, B. J.; Toussaint, J.; Lindeman, S. V.; Bennett, B.; Gardinier, J. R. *Dalton Trans.* **2011**, *40*, 8776−8787. (e) Wanniarachchi, S.; Liddle, B. J.; Toussaint, J.; Lindeman, S. V.; Bennett, B.; Gardinier, J. R. *Dalton Trans.* **2010**, *39*, 3167−3169.

(20) CrysAlisPro, Agilent Technologies,Version 1.171.34.46 (release 25-11-2010 CrysAlis171.NET), compiled Nov 25 2010,17:55:46.

(21) *SAINT+ Version 7.23a and SADABS Version 2004/1*; Bruker Analytical Xray Systems, Inc.: Madison, WI, 2005.

(22) Sheldrick, G. M. *SHELXTL Version 6.12*; Bruker Analytical X-ray Systems, Inc.: Madison, WI, 2001.

(23) *SCALE3 ABSPACK - An Oxford Diffraction program (1.0.4,gui:1.0.3) (C)*; Oxford Diffraction Ltd., 2005.

(24) As per a reviewer's query, it has not yet proven possible to isolate pure heteroleptic (X,Y)NiCl complexes from the dark green reaction mixtures obtained when using equimolar quantities of $NiCl_2$, pincer ligand, and base. Instead, the orange symmetrized product, $Ni(X,Y)_2$, is recovered from such attempts after solvent removal. Further efforts in this vein, using sterically encumbered pincer variants, are underway, and results will be reported in due course.

(25) The single-crystal diffraction study of $3{\cdot}CH_2Cl_2$ shows a layered supramolecular structure where molecules of **3** are held together by CH···π and π···π noncovalent interactions. The solvate molecules are retained between sheets with [(solvate)CH···π (aryl) and (pz)CH···Cl] noncovalent interactions. It can be speculated that similar noncovalent interactions may be involved in the capture and retention of water molecules. Unfortunately, we were unsuccessful at completely removing solvent from $3{\cdot}CH_2Cl_2$, and because adventitious water replaces CH_2Cl_2 in dried samples, it is simply easier to work with the hemihydrate.

(26) Lever, A. B. P. *Inorg. Chem.* **1965**, *4*, 763−764.

(27) (a) Renger, T. *Phys. Rev. Lett.* **2004**, *93*, 188101-1−188101-4. (b) Holmes, O. G.; McClure, D. S. *J. Chem. Phys.* **1957**, *26*, 1686−1694.

(28) (a) Patra, A. K.; Mukherjee, R. *Inorg. Chem.* **1999**, *38*, 1388−1393. (b) Mueller, H.; Bauer-Siebenlist, B.; Csapo, E.; Dechert, S.; Farkas, E.; Meyer, F. *Inorg. Chem.* **2008**, *47*, 5278−5292. (c) Michaud, A.; Fontaine, F.-G.; Zargarian, D. *Acta Crystallogr.* **2005**, *E61*, m784−m786. (d) Hirotsu, M.; Tsukahara, Y.; Kinoshita, I. *Bull. Chem. Soc. Jpn.* **2010**, *83*, 1058−1066. (e) Baker, A. T.; Craig, D. C.; Rae, A. D. *Aust. J. Chem.* **1995**, *48*, 1373−1378. (f) Astley, T.; Gulbis, J. M.; Hitchman, M. A.; Tiekink, E. R. T. *J. Chem. Soc., Dalton Trans.* **1993**, 509−515. (g) Reimann, C. W. *J. Phys. Chem.* **1970**, *74*, 561−568.

(29) Kasha, M.; Rawls, R. *Photochem. Photobiol.* **1968**, *7*, 561.

(30) Hansch, C.; Leo, A.; Taft, R. W. *Chem. Rev.* **1991**, *91*, 165−195.

(31) (a) McDaniel, A. M.; Rappé, A. K.; Shores, M. P. *Inorg. Chem.* **2012**, *51*, 12493−12502. (b) Sasaki, Y. *Bull. Inst. Chem. Res., Kyoto Univ.* **1980**, *58*, 187−192. (c) Robinson, M. A.; Curry, J. R.; Busch, D. B. *Inorg. Chem.* **1963**, *2*, 1178−1181.

(32) (a) DeAlwis, D. C. L.; Schulz, F. A. *Inorg. Chem.* **2003**, *42*, 3616−3622. (b) Nolet, M. C.; Michaud, A.; Bain, C.; Zargarian, D.; Reber, C. *Photochem. Photobiol.* **2006**, *82*, 57−63.

(33) The independence of lowest energy NIR transition and the nature of *para*-aryl substituents indicate that the LUMO must also contain substantial ligand character.

(34) (a) Crutchley, R. J. *Adv. Inorg. Chem.* **1994**, *41*, 273−325. (b) Zanello, P. *Inorganic Electrochemistry: Theory, Practice and Applications*; Royal Society of Chemistry: Cambridge, 2003; pp 174−178. (c) Astruc, D. *Electron Transfer and Radical Processes in Transition-Metal Chemistry*; VCH Publishers, Inc.: New York, 1995; pp 34−36.

(35) Winter, R. F. *Organometallics* **2014**, Article ASAP, DOI: 10.1021/om500029x.

(36) (a) Luo, S.; Averkiev, B.; Yang, K. R.; Xu, X.; Truhlar, D. G. *J. Chem. Theory Comput.* **2014**, *10*, 102−121. (b) Neese, F. *J. Phys. Chem. Solids* **2004**, *65*, 781−785. (c) Ruiz, E.; Cano, J.; Alvarez, S.; Alemany, P. *J. Comput. Chem.* **1999**, *20*, 1391−1400. (d) Caballol, R.; Castell, O.; Illas, F.; Moreira, I.; de, P. R.; Malrieu. *J. Phys. Chem. A* **1997**, *101*, 7860−7866. (e) Noodleman, L. *J. Chem. Phys.* **1981**, *74*, 5737−5743.

(37) (a) Hush, N. S. *Prog. Inorg. Chem.* **1967**, *8*, 391−444. (b) Hush, N. S. *Coord. Chem. Rev.* **1985**, *64*, 135−157.

(38) A reviewer noted that the N···N distance might not be the best distance to describe the electronic coupling because the charge was delocalized over the ligand via the quinoidal distortion. If the *d* value is changed to 8.425 Å, which is an estimate of the longest aryl−aryl centroid−centroid distance in $(\mathbf{1})^+$ from experimental structures of **1** and $(\mathbf{1})^{2+}$, then H_{ab} of **1** is reduced to 226 cm^{-1}, and this value would represent a lower limit of electronic coupling strength. A similar calculation on the gallium complex gives H_{ab} = 125 cm^{-1}. Regardless, the conclusions derived from calculations using either *d* value remain the same.

(39) These values are slightly different than those reported in ref 19a. There was a typographical error in the $E_{1/2}(1)$ entry of Table 1 of the previous publication, which should read 0.989(3) instead of 0.939(3).

(40) Brunschwig, B. S.; Creutz, C.; Sutin, N. *Chem. Soc. Rev.* **2002**, *31*, 168−184.

(41) Marcus, R. A.; Sutin, N. *Biochim. Biophys. Acta* **1985**, *811*, 265−322. (b) Sutin, N. *Prog. Inorg. Chem.* **1983**, *30*, 441−499.
(42) Stoll, S.; Schweiger, A. *J. Magn. Reson.* **2006**, *178*, 42−55.
(43) (a) Mann, J. B.; Meek, T. L.; Knight, E. T.; Capitani, J. F.; Allen, L. C. *J. Am. Chem. Soc.* **2000**, *122*, 5132−5137. (b) Mann, J. B.; Meek, T. L.; Allen, L. C. *J. Am. Chem. Soc.* **2000**, *122*, 2780−2783.